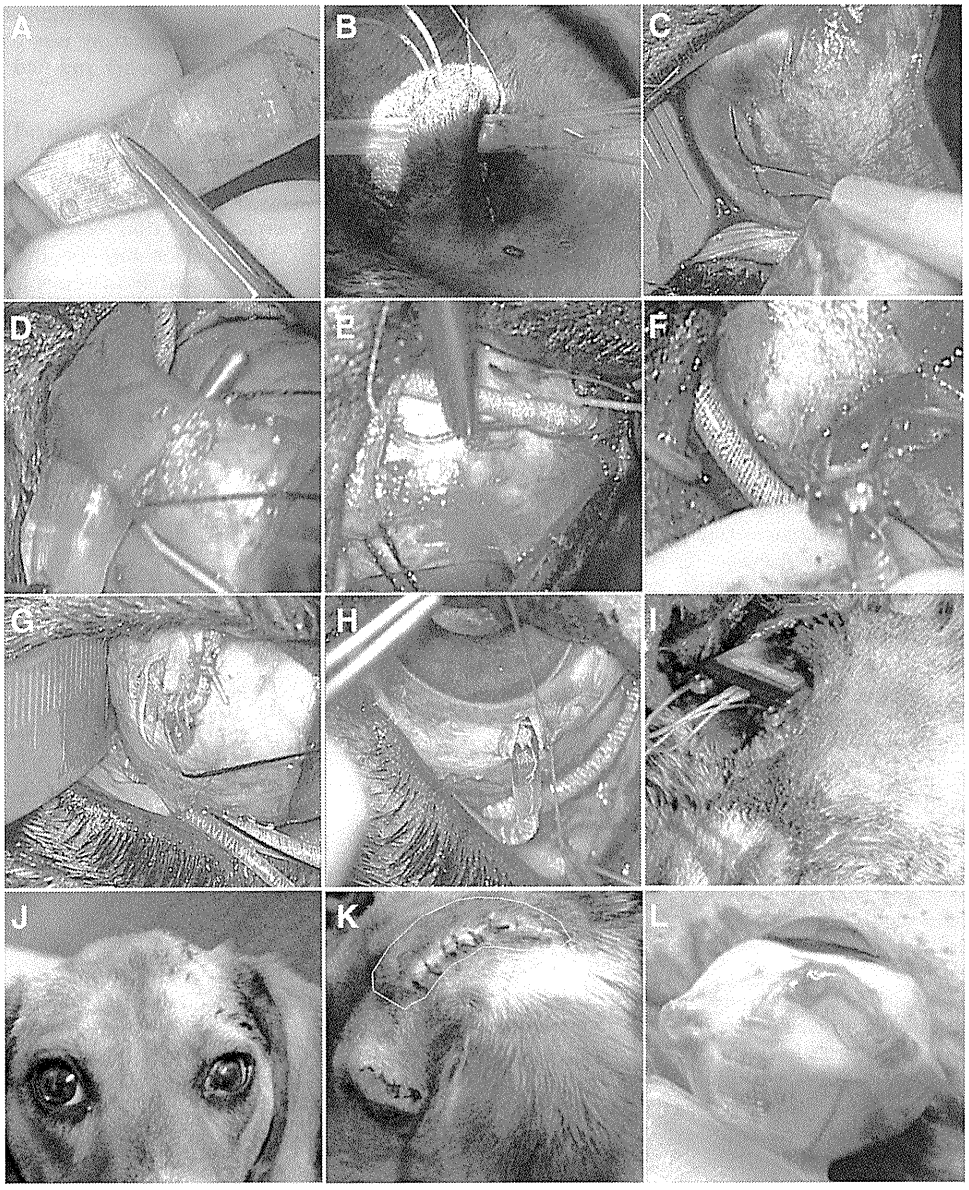


**FIGURE 2.** Photographs taken during implantation surgery and 1 month after implantation. (**A**) Microelectrode array and return electrode are combined into one bundle and covered with silicone rubber tubing. (**B**) Customized trocar and electrodes. (**C**) Creation of a scleral pocket. (**D**) Electrodes and cables are passed under an extraocular muscle. (**E**) Cable is sutured to the sclera. (**F**) Insertion of a return electrode. (**G**) An electrode array was inserted into the scleral pocket, and the cable was sutured to the sclera. (**H**) Return electrode inserted intravitreally and sutured to the sclera. (**I**) Extraocular microstimulator implanted on the surface of the left temporal muscle. (**J**) Frontal view of dog 1 month after implantation. The position of the eye is orthophoric. (**K**) Temporal view of dog 1 month after implantation. All wounds have healed properly, and no sign of infections or wound dehiscence can be seen. The position of the extraocular stimulator was surrounded with the *white line*. (**L**) An enucleated eye that has an electrode array implanted into the scleral pocket.

trocar (Fig. 2B).[24,29] The devices and cables were passed through the tunnel under the superior muscle, and the silicone rubber protector was removed to separate the microelectrode array and the return electrode.

A scleral pocket (7 mm × 7 mm) was made in the superotemporal or superonasal quadrant approximately 10 to 12 mm posterior to the limbus (Fig. 2C). The cable connecting the array was passed under the other rectus muscles and sutured to the sclera (Figs. 2D, 2E). The other cable connected to the return electrode was also passed under the other rectus and was sutured to the sclera after the insertion of the return electrode into the vitreous cavity (Fig. 2F).

After implantation of the electrodes (Figs. 2G, 2H), the extraocular stimulator was tightly sutured to the temporal muscle, and the incisions on the head and the brow were sutured (Fig. 2I).

## Fundus Photography and Fluorescein Angiography

Color fundus photographs were taken under general anesthesia before surgery and monthly after surgery. Fluorescein angiography (FA) was performed at 1 month and 3 months after surgery. For both procedures, the eyes were dilated with topical 2.5% phenylephrine hydrochloride and 0.5% tropicamide (Midrine P; Santen Co., Ltd., Osaka, Japan), and fundus photographs were taken with a fundus camera (TRC-50IX; Topcon Corporation, Tokyo, Japan). For FA, photographs were taken after the injection of 0.075 mL/kg of 10% sodium fluorescein solution (Fluorescite; Alcon Japan Ltd., Tokyo, Japan) into a vein.

## Electroretinography

Bright-light flash electroretinograms were recorded 3 months after the implantation of the STS electrode array. Under general anesthesia, the pupils were dilated with 2.5% phenylephrine hydrochloride and 0.5% tropicamide, and a 2.5% hydroxypropyl methylcellulose ophthalmic solution (Scopysol; Santen Co. Ltd., Osaka, Japan) was used with a corneal contact lens electrode/LED mini-Ganzfeld stimulator (WLS-20; Mayo Corporation, Nagoya, Japan). A reference electrode was inserted subdermally into the left ear, and a ground electrode was inserted subdermally into the nose. The animal was dark-adapted for 30 minutes before the electroretinographic (ERG) recordings. Responses elicited by bright flash stimuli (1.5 log cd · s/m$^2$) were amplified, band pass filtered from 0.3 to 1000 Hz, and digitized at 3.3 kHz. Five responses were averaged with an interstimulus interval of 10 seconds on a

computational ERG recording system (Neuropack μ; Nihon Kohden, Tokyo, Japan).

### Functional Testing of STS System

To confirm the integrity and stability of the STS system, functional testing of the STS system was performed. The voltage in the microelectronic circuit of the extraocular stimulator was measured by another circuit as a comparator inside the extraocular stimulator. The maximum voltage of this circuit was 10.0 V, and we set 9.5 V as a saturation voltage. Just after implantation and then at 1, 2, and 3 months after implantation, we checked to be sure that the voltage did not exceed the saturation voltage of 9.5 V. Each of the nine active electrodes was activated with balanced, cathodic-first biphasic pulses of 200 to 1000 μA, with a duration of 0.5 ms/phase and pulse duration of 0.5 ms. The frequency of the pulses was 20 Hz for 0.5 seconds that was controlled by the extraocular stimulator driven by the extracorporeal transmitter. If the voltage in the electric circuit in the microstimulator was less than the saturation voltage, the device set the current as pass, but if the voltage exceeded the saturation voltage, the device set the current as failure.

Next the artifacts evoked by electrical stimulation were recorded with a contact lens corneal electrode/LED mini-Ganzfeld stimulator (WLS-20; Mayo Corporation). A reference electrode was inserted subdermally into the left ear, and a ground electrode was inserted subdermally into the nose. Responses elicited by electrical stimulation were amplified and band pass filtered from 0.3 to 1000 Hz, and the responses were digitized at 3.3 kHz. One response was recorded using a computational ERG recording system (Neuropack μ; Nihon Kohden).

### Histologic Analyses

After 3 months, the animals were euthanatized with 120 mg/kg intravenous pentobarbital (Somunopentyl; Kyoritsu Seiyaku Corporation) while the animals were under general anesthesia. Both eyes were enucleated, after which the electrodes and cables were removed from the left eyes. Then the eyes were placed in 1.2% glutaraldehyde and 2% paraformaldehyde in 0.1 M phosphate buffer (PB) for 30 minutes at room temperature. Eyes were trimmed, and the eyecup with the optic nerve was postfixed in the fixative at 4°C for 24 hours. The eyecups were kept in 10% formaldehyde in 0.1 M phosphate buffer at 4°C for 24 hours. Tissues were trimmed and embedded in paraffin. Semithin sections (4.0 μm) were cut along the meridian, including the optic disc and the electrode array, and were stained with hematoxylin and eosin for light microscopy.

## Results

### Results of Implantation Surgery

Results of the implantation surgery are shown in Figure 2. All prostheses were safely implanted, and no intraoperative complications were encountered. The shape of the extraocular stimulator fit the curve of the head, and the electrode array and the return electrode could be easily passed under the skin from the temporal muscle into the orbit with the customized trocar. The cable easily encircled the globe, and the electrode array and the return electrode could be easily inserted (Figs. 2G, 2H). No severe bleeding occurred during the creation of the scleral pocket and the insertion of the needle electrode.

The position of the eyes was maintained orthophoric without proptosis (Fig. 2J). All the wounds healed properly, and no sign of infections or wound dehiscence could be seen (Fig. 2K). The fixation of the extraocular stimulator was also stable throughout the observation period in all cases (Fig. 2K). The animals moved freely in their kennels and showed no apparent alterations in behavior.

Three months after implantation, the animals were deeply anesthetized and the eyes were enucleated. The fixation of the electrode array and the cable was examined macroscopically. The electrode array was found to be completely inserted into the sclera pocket and had not rotated on its axis (Fig. 2L).

### Postoperative FA and Ophthalmic Examinations

Immediately after surgery, moderate edema and hematomas were noticeable in the periorbital region. Conjunctival chemosis and injection were also observed in all cases. Approximately 7 days after surgery, the conjunctival chemosis, periorbital edema, and hematoma had almost completely resolved. All wounds healed properly, and no signs of infections or wound dehiscence were noticed.

Ophthalmic examinations showed that there were no ocular complications, infections, retinal detachment, or vitreous or subretinal hemorrhages. A localized posterior subcapsular cataract was present in dog 2 that was probably caused by the needle electrode touching the lens; however, the opacification did not get worse.

Fundus photographs of the three dogs are shown in Figure 3. In dog 1, the implanted electrode array was not detectable, and there was no obvious indication of surgical damage or side effects (Figs. 3A, 3C). In dogs 2 and 3, the notch of the electrode array and the outline of the array were detected 1 month after implantation (Figs. 3E, 3I; white and black arrowheads). In addition, pigmentation of the retina at the edge of the array distal to the cable was observed in dog 2 (Fig. 3I). The size of the pigmented area did not change throughout the 3-month observation period (Fig. 3K).

FA showed intact vasculature without signs of inflammation, leakage, obstruction, or formation of new vessels in the area overlying and surrounding the implant in all dogs (Figs. 3B, 3D, 3F, 3H). In dog 2, there was no detectable sign of retinal damage at the pigmented area (Figs. 3J, 3L).

### Electroretinography

The electroretinograms had normal a-wave and b-waves, and the shapes did not differ from those of electroretinograms recorded from the unoperated fellow eye 3 months after implantation in all three animals (Fig. 4, Table 1).

### Functional Testing of STS System

The voltage in the microelectronic circuit of the extraocular stimulator was less than the saturation voltage in all electrodes and in all cases throughout the observation period (data not shown). Representative stimulus artifact waveforms recorded with a contact lens electrode are shown in Figure 5. All the electrodes could deliver the electric currents (Figs. 5A, 5B). Pattern stimulation could also be performed as shown in Figures 5C to 5F. The amplitude of the artifacts was altered by the current intensity (Figs. 5E, 5F).

### Histologic Analyses

Sections from two implanted and control eyes showed no obvious changes in the structure of the retina and the choroid beneath the electrode array in dogs 1 and 3 (Figs. 6A, 6C). Although the notch of the electrode array was not visible in dog 1, the electrode array was completely inserted in the scleral pocket (Fig. 6A). On the other hand, pathologic changes were detected in the retina of dog 2. Although the changes were limited to the edge of the array, the retinal and choroidal architecture was destroyed because of the mechanical pressure of the array (Figs. 6B, 6D; black arrowheads). However, there was no obvious damage at other regions of the retina beneath the array (Figs. 6B, 6D; black arrows).

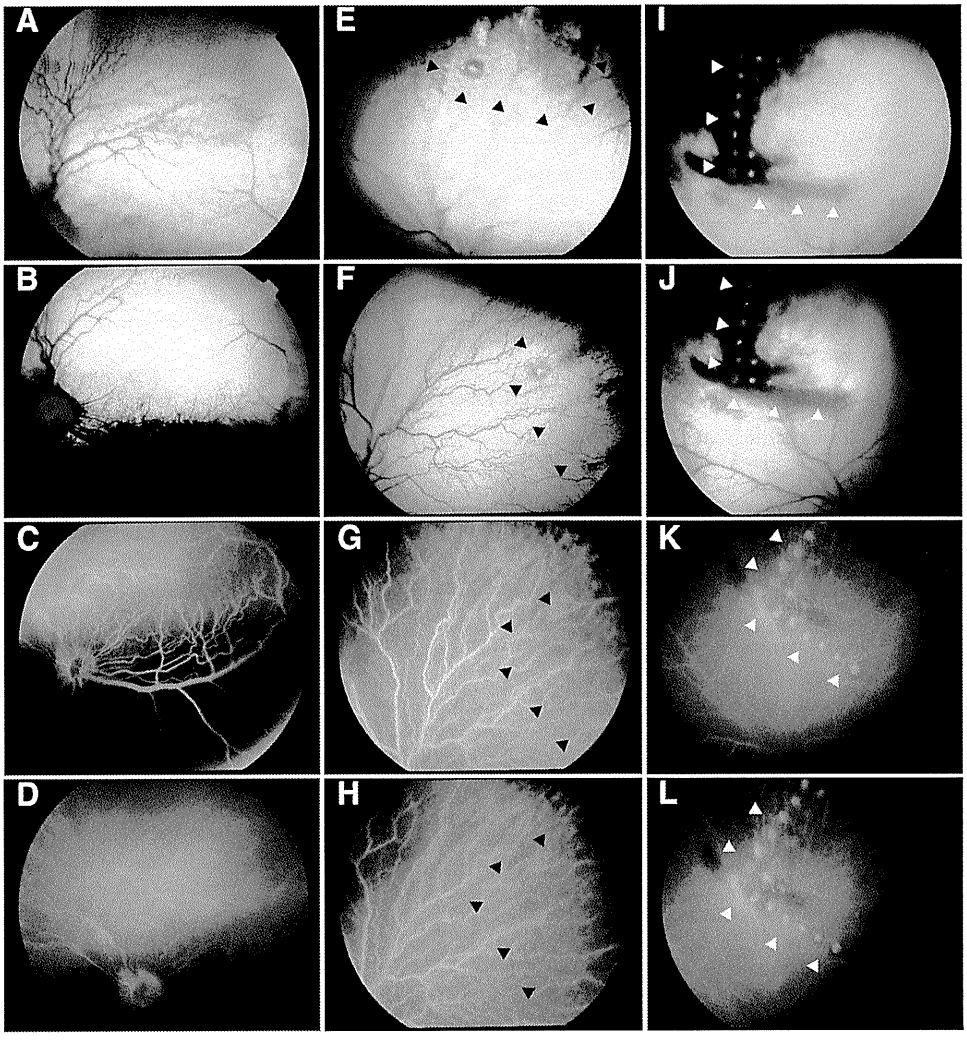


**Figure 3.** Fundus photographs and fluorescein angiograms 1 month and 3 months after implantation in three dogs. (**A–D**) The retina appears normal, with no evidence of the STS electrode array implanted in dog 1. (**A, C**) One month after implantation. (**B, D**) Three months after implantation. (**E–H**) Photographs of dog 3. Although the notch of the electrode array can be seen (*black arrowheads*), there are no significant changes such as inflammation, retinal obstruction, and vascular damage throughout the observation period. (**E–G**) One month after implantation. (**F–H**) Three months after implantation. (**I–L**) Photographs of dog 2. Although pigmentation of the retina can be seen at the implantation site (*white arrowheads*), there is no severe retinal damage around the array. (**I, K**) One month after implantation. (**J, L**) Three months after implantation.

## Discussion

Our results showed that it is possible to implant our STS device into the deep lamellar scleral space of beagle dogs without intraoperative or postoperative complications and that the system was biocompatible with the tissue and remained stable for 3 months. This is the first report of successful implantation of an STS device consisting of electrodes and an extraocular microstimulator and demonstrates that this device operated normally for the 3-month experimental period.

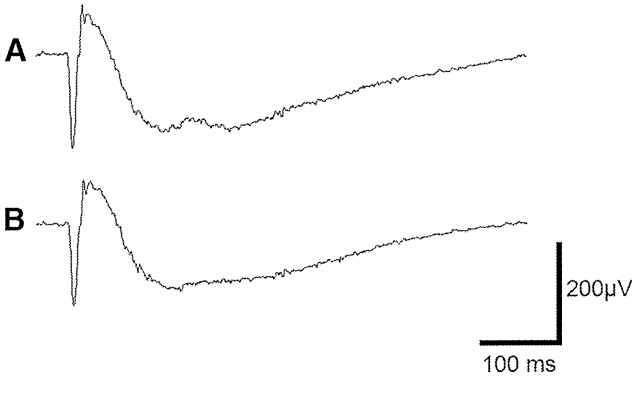


**Figure 4.** Three months after implantation. Representative electroretinograms recorded of the implanted eye (**A**) and fellow eye (**B**) of dog 1.

### Feasibility of Implanting STS System Device

The surgery was successful in all cases and led to stable placement of the prosthesis over the 3-month period. Although the device was designed to be implanted into humans, the shapes of the microstimulator and the electrodes fit the anatomy and tissues of the dog very well. It was not difficult to pass the electrodes from the head region to the eye, though our internal device was divided into electrodes and extraocular microstimulator because we used a customized trocar similar to that used by Gekkeler et al.[24] and Besch et al.[29] The electrodes and cables were first enclosed in a silicone cover and passed through the trocar to the surface of the eye. The length of the cable was sufficient, and its flexibility was good for the implantation surgery.

In one animal, the retina at the edge of the electrode array distal to the cable was histologically degenerated, though this degeneration did not spread. Because the scleral incision was made only to the surface of the outer choroid, the local circulation of the choroid at the edge of the array might have been damaged. This taught us that it is critical to control the depth of the scleral pocket to avoid retinal and choroidal damage.

TABLE 1. Amplitudes and Latencies of Electroretinograms of 3 Dogs

| | Left Eye (operated) | | | | Right Eye (unoperated) | | | |
|---|---|---|---|---|---|---|---|---|
| | a-Wave | | b-Wave | | a-Wave | | b-Wave | |
| Dog | Amp (μV) | Latency (ms) | Amp (μV) | Latency (ms) | Amp (μV) | Latency (ms) | Amp (μV) | Latency (ms) |
| 1 | 170 | 44.7 | 264 | 56.7 | 144 | 45.0 | 225 | 57.6 |
| 2 | 233 | 45.0 | 383 | 69.3 | 270 | 46.5 | 484 | 70.5 |
| 3 | 118 | 45.0 | 244 | 73.8 | 82.7 | 45.3 | 215 | 71.1 |

Amp, amplitude.

## Biocompatibility and Stability of STS Device

No major undesirable reactions such as cellular proliferation, inflammation, or retention of subretinal fluid in the retina beneath the electrode array occurred during the experimental period. These results are similar to our findings in rabbits.[38,39] ERG studies showed no significant decline of retinal function compared with the electroretinograms in the control eyes, indicating good biocompatibility of the implanted STS system in dogs.

We also checked whether the voltage in the circuit in the microstimulator was greater than the saturation voltage to examine the stability of the STS device. Although the voltage evoked by each of the nine electrodes was less than the saturation voltage, we could not measure the actual voltage from nine electrodes because of the recording system. Therefore, we could not detect any significant difference in the amplitude of the voltage among these electrodes to check which electrode made good contact with the tissue or whether it was damaged.

We recorded the artifacts evoked by electrical pulses and considered these electrical changes as an indication of the function of an STS system, as did Yamauchi et al.,[45] because it was difficult to record the electrical-evoked potentials on the surface of the visual area of the brain. These results indicated good stability of the STS system device after implantation.

## Comparison with Other Retinal Prostheses

It has still not been determined which approach—epiretinal, subretinal, optic nerve, or suprachoroidal—will provide the best functional outcomes. To avoid the invasive surgery required to implant the epiretinal, subretinal, and optic nerve electrodes, we chose the suprachoroidal position for the electrode array. Subretinal implantation requires more complex surgery and requires a transscleral approach. With this method, the electrode array would have to pass through the choroid to the subretinal space, and it is possible that this would result in ocular complications such as retinal detachments, choroidal hemorrhages, and endophthalmitis. The epiretinal prosthesis is not difficult to place on the retina; however, the epiretinal implants and cables must pass through the pars plana and vitreous and be placed directly on the retina. Therefore, vitreous hemorrhage, retinal detachment, endophthalmitis, and retinal damage can develop. The optic nerve prosthesis requires complex surgery because it is necessary to insert the electrodes into the optic nerve, and the number of electrodes is limited by the size of the orbital space.

On the other hand, the surgical technique for implantation of the STS system is relatively simple and is less invasive because the electrode array is implanted into the deep lamellar scleral space away from the retina. In addition, the surgical difficulties of removing or replacing the electrodes are less traumatic than those necessary for the other types of prostheses. However, the estimated spatial resolution for the STS prosthesis is approximately 1° of visual angle,[36] which is not as good as that of subretinal stimulation or epiretinal stimulation.[38,39]

Although the threshold current by STS is slightly higher than that for the other types of prostheses,[41] the current is

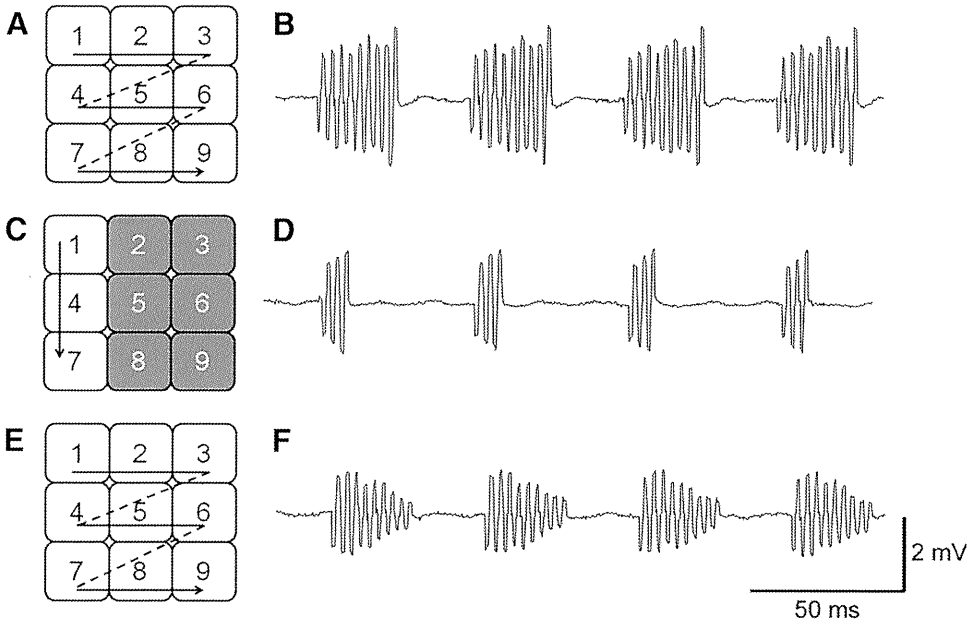


FIGURE 5. Three months after implantation. Representative waveforms of the stimulus artifacts of dog 3. Drawing of the stimulus pattern of electrodes (A) and waveforms of artifacts derived from each of nine electrodes (electrodes 1–9) sequentially. Nine waves are shown (B). Drawing of stimulus pattern (C) and waveforms of artifacts derived from three electrodes (electrodes 1, 4, 7). Three waves can be seen (D). Drawing of stimulus pattern (E) and waveforms of artifacts derived from nine electrodes with different electric current intensity (electrodes 1 [1 mA], 2 [0.9 mA], 3 [0.8 mA], 9 [0.2 mA]). Amplitudes of artifacts increase with increasing current intensity (F).

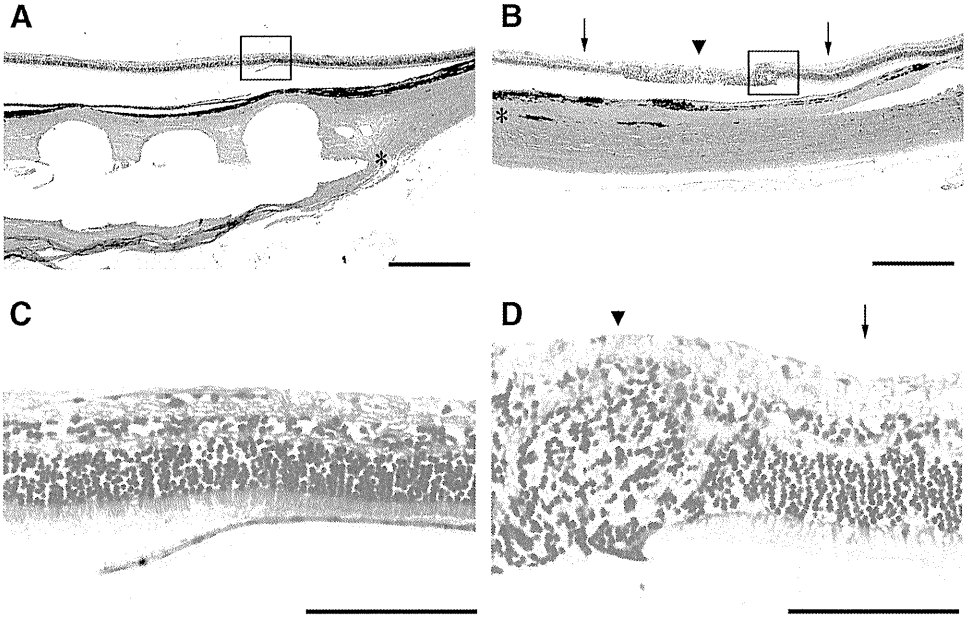


FIGURE 6. Light microscopic photographs of the retina and sclera of the implanted eyes. (**A**, **C**) Photographs of the retina and sclera around the electrode array of dog 1. There is no obvious change in the structure of the retina and the choroid around the array. Magnifications: (**A**) ×40; (**C**) ×400. (**B**, **D**) Photographs of the retina and sclera around the array of dog 2. Local damage to the retina and choroid at the site of the implanted electrode array can be seen (*arrowheads*); however, other areas of the retina on the array are intact (*arrows*). Magnifications: (**B**) ×40; (**D**) ×400. Scale bars: (**A**, **B**) ×500 μm; (**C**, **D**) 100 μm. (*asterisk*) Edge of the array distal to the cable.

within the safe limits for long-term stimulation.[27] In addition, Shivdasani et al.[46] suggested that it was possible to reduce voltage requirements for the STS system by selecting the proper electrical parameters.

## STS Device

Our electrode array had 49 potential electrodes, but only nine were active in this study. We are developing a complete STS device with 49 active electrodes. We plan to implant this STS device into animals and to observe the animals for a longer period.

## Conclusion

In conclusion, the aim of this study was to determine the feasibility of implanting our STS system into animals with larger eyes and to determine compatibility and stability over a 3-month period. We successfully implanted a newly developed STS prosthesis in the deep lamellar scleral space of beagle dogs. The implanted STS prosthesis was biocompatible and remained stable for at least 3 months. Further investigations are needed to rule out any influence of chronic electrical stimulation provided by this STS system on its biocompatibility and stability for a longer term follow-up.

## *Acknowledgments*

The authors thank their project partners Kouji Oosawa, Eiji Yonezawa, Yasuo Terasawa, and Tohru Saitoh (Vision Institution, Nidek Co., Ltd.) for their help.

## *References*

1. Hartong DT, Berson EL, Dryja TP. Retinitis pigmentosa. *Lancet.* 2006;368:1795–1809.
2. Heckenlively JR. RP syndromes. In: Heckenlively JR, ed. *Retinitis Pigmentosa*. Philadelphia: JB Lippincott; 1988;221–252.
3. Daiger SP, Bowne SJ, Sullivan LS. Perspective on genes and mutations causing retinitis pigmentosa. *Arch Ophthalmol.* 2007;125: 151–158.
4. Pagon RA. Retinitis pigmentosa. *Surv Ophthalmol.* 1988;33:137–177.
5. Marmor MF. Visual loss in retinitis pigmentosa. *Am J Ophthalmol.* 1980;89:692–698.
6. Madreperla SA, Palmer RW, Massof RW, Finkelstein D. Visual acuity loss in retinitis pigmentosa: relationship to visual field loss. *Arch Ophthalmol.* 1990;108:358–361.
7. Zrenner E, Miliczek KD, Gabel VP, et al. The development of subretinal microphotodiodes for replacement of degenerated photoreceptors. *Ophthalmic Res.* 1997;29:269–280.
8. Rizzo JF 3rd, Wyatt J, Humayun M, et al. Retinal prosthesis: an encouraging first decade with major challenges ahead. *Ophthalmology.* 2001;108:13–14.
9. Margalit E, Maia M, Weiland JD, et al. Retinal prosthesis for the blind. *Surv Ophthalmol.* 2002;47:335–356.
10. Lakhanpal RR, Yanai D, Weiland JD, et al. Advances in the development of visual prostheses. *Curr Opin Ophthalmol.* 2003;14: 122–127.
11. Sachs HG, Gabel VP. Retinal replacement: the development of microelectronic retinal prostheses—experience with subretinal implants and new aspects. *Graefes Arch Clin Exp Ophthalmol.* 2004;242:717–723.
12. Loewenstein JI, Montezuma SR, Rizzo JF 3rd. Outer retinal degeneration: an electronic retinal prosthesis as a treatment strategy. *Arch Ophthalmol.* 2004;122:587–596.
13. Fernández E, Pelayo F, Romero S, et al. Development of a cortical visual neuroprosthesis for the blind: the relevance of neuroplasticity. *J Neural Eng.* 2005;2:R1–R12.
14. Bertschinger DR, Beknazar E, Simonutti M, et al. A review of in vivo animal studies in retinal prosthesis research. *Graefes Arch Clin Exp Ophthalmol.* 2008;246:1505–1517.
15. Chader GJ, Weiland J, Humayun MS. Artificial vision: needs, functioning, and testing of a retinal electronic prosthesis. *Prog Brain Res.* 2009;175:317–332.
16. Majji AB, Humayun MS, Weiland JD, et al. Long-term histological and electrophysiological results of an inactive epiretinal electrode array implantation in dogs. *Invest Ophthalmol Vis Sci.* 1999;40: 2073–2081.
17. Schwahn HN, Gekeler F, Kohler K, et al. Studies on the feasibility of a subretinal visual prosthesis: data from Yucatan micropig and rabbit. *Graefes Arch Clin Exp Ophthalmol.* 2001;239:961–967.
18. Völker M, Shinoda K, Sachs H, et al. In vivo assessment of subretinally implanted microphotodiode arrays in cats by optical coherence tomography and fluorescein angiography. *Graefes Arch Clin Exp Ophthalmol.* 2004;242:792–799.
19. Chow AY, Chow VY, Packo KH, , et al. The artificial silicon retina microchip for the treatment of vision loss from retinitis pigmentosa. *Arch Ophthalmol.* 2004;122:460–469.

20. Güven D, Weiland JD, Fujii G, et al. Long-term stimulation by active epiretinal implants in normal and RCD1 dogs. *J Neural Eng.* 2005;2:S65–S73.
21. Fang X, Sakaguchi H, Fujikado T, et al. Direct stimulation of optic nerve by electrodes implanted in optic disc of rabbit eyes. *Graefes Arch Clin Exp Ophthalmol.* 2005;243:49–56.
22. Montezuma SR, Loewenstein J, Scholz C, Rizzo JF 3rd. Biocompatibility of materials implanted into the subretinal space of Yucatan pigs. *Invest Ophthalmol Vis Sci.* 2006;47:3514–3522.
23. Colodetti L, Weiland JD, Colodetti S, et al. Pathology of damaging electrical stimulation in the retina. *Exp Eye Res.* 2007;85:23–33.
24. Gekeler F, Szurman P, Grisanti S, et al. Compound subretinal prostheses with extra-ocular parts designed for human trials: successful long-term implantation in pigs. *Graefes Arch Clin Exp Ophthalmol.* 2007;245:230–241.
25. Veraart C, Raftopoulos C, Mortimer JT, et al. Visual sensations produced by optic nerve stimulation using an implanted self-sizing spiral cuff electrode. *Brain Res.* 1998;813:181–186.
26. Delbeke J, Oozeer M, Veraart C. Position, size and luminosity of phosphenes generated by direct optic nerve stimulation. *Vision Res.* 2003;43:1091–1102.
27. Humayun MS, Weiland JD, Fujii GY, et al. Visual perception in a blind subject with a chronic microelectronic retinal prosthesis. *Vision Res.* 2003;43:2573–2581.
28. Rizzo JF 3rd, Wyatt J, Loewenstein J, Kelly S, Shire D. Perceptual efficacy of electrical stimulation of human retina with a microelectrode array during short-term surgical trials. *Invest Ophthalmol Vis Sci.* 2003;44:5362–5369.
29. Besch D, Sachs H, Szurman P, et al. Extraocular surgery for implantation of an active subretinal visual prosthesis with external connections: feasibility and outcome in seven patients. *Br J Ophthalmol.* 2008;92:1361–1368.
30. Horsager A, Greenwald SH, Weiland JD, et al. Predicting visual sensitivity in retinal prosthesis patients. *Invest Ophthalmol Vis Sci.* 2009;50:1483–1491.
31. Sakaguchi H, Kamei M, Fujikado T, et al. Artificial vision by direct optic nerve electrode (AV-DONE) implantation in a blind patient with retinitis pigmentosa. *J Artif Organs.* 2009;12:206–209.
32. Humayun MS, Dorn JD, Ahuja AK, et al. Preliminary 6 month results from the Argus II epiretinal prosthesis feasibility study. *Conf Proc IEEE Eng Med Biol Soc.* 2009;2009:4566–4568.
33. Brelén ME, Vince V, Gérard B, Veraart C, Delbeke J. Measurement of evoked potentials after electrical stimulation of the human optic nerve. *Invest Ophthalmol Vis Sci.* 2010;51:5351–5355.
34. Benav H, Bartz-Schmidt KU, Besch D, et al. Restoration of useful vision up to letter recognition capabilities using subretinal microphotodiodes. *Conf Proc IEEE Eng Med Biol Soc.* 2010;2010:5919–5922.
35. Horsager A, Boynton GM, Greenberg RJ, Fine I. Temporal interactions during paired-electrode stimulation in two retinal prosthesis subjects. *Invest Ophthalmol Vis Sci.* 2011;52:549–557.
36. Kanda H, Morimoto T, Fujikado T, et al. Electrophysiological studies of the feasibility of suprachoroidal-transretinal stimulation for artificial vision in normal and RCS rats. *Invest Ophthalmol Vis Sci.* 2004;45:560–566.
37. Sakaguchi H, Fujikado T, Kanda H, et al. Electrical stimulation with a needle-type electrode inserted into the optic nerve in rabbit eyes. *Jpn J Ophthalmol.* 2004;48:552–557.
38. Nakauchi K, Fujikado T, Kanda H, et al. Transretinal electrical stimulation by an intrascleral multichannel electrode array in rabbit eyes. *Graefes Arch Clin Exp Ophthalmol.* 2005;243:169–174.
39. Nakauchi K, Fujikado T, Kanda H, et al. Threshold suprachoroidal-transretinal stimulation current resulting in retinal damage in rabbits. *J Neural Eng.* 2007;4:S50–S57.
40. Nishida K, Kamei M, Kondo M, et al. Efficacy of suprachoroidal-transretinal stimulation in a rabbit model of retinal degeneration. *Invest Ophthalmol Vis Sci.* 2010;51:2263–2268.
41. Fujikado T, Morimoto T, Kanda H, et al. Evaluation of phosphenes elicited by extraocular stimulation in normals and by suprachoroidal-transretinal stimulation in patients with retinitis pigmentosa. *Graefes Arch Clin Exp Ophthalmol.* 2007;245:1411–1419.
42. Tokuda T, Asano R, Sugitani S, et al. In vivo stimulation on rabbit retina using CMOS LSI-based multi-chip flexible stimulator for retinal prosthesis. *Conf Proc IEEE Eng Med Biol Soc.* 2007;5791–5794.
43. Ohta J, Tokuda T, Kagawa K, et al. Laboratory investigation of microelectronics-based stimulators for large-scale suprachoroidal transretinal stimulation (STS). *J Neural Eng.* 2007;4:S85–S91.
44. Terasawa Y, Uehara A, Yonezawa E, et al. A visual prosthesis with 100 electrodes featuring wireless signals and wireless power transmission. *IEICE Electronics Express.* 2008;5:574–580.
45. Yamauchi Y, Franco LM, Jackson DJ, et al. Comparison of electrically evoked cortical potential thresholds generated with subretinal or suprachoroidal placement of a microelectrode array in the rabbit. *J Neural Eng.* 2005;2:S48–S56.
46. Shivdasani MN, Luu CD, Cicione R, et al. Evaluation of stimulus parameters and electrode geometry for an effective suprachoroidal retinal prosthesis. *J Neural Eng.* 2010;7:036008.

# Identification of Autoantibodies against TRPM1 in Patients with Paraneoplastic Retinopathy Associated with ON Bipolar Cell Dysfunction

**Mineo Kondo[1*]**, **Rikako Sanuki[2,3]**, **Shinji Ueno[1]**, **Yuji Nishizawa[4]**, **Naozumi Hashimoto[5]**, **Hiroshi Ohguro[6]**, **Shuichi Yamamoto[7]**, **Shigeki Machida[8]**, **Hiroko Terasaki[1]**, **Grazyna Adamus[9]**, **Takahisa Furukawa[2,3*]**

**1** Department of Ophthalmology, Nagoya University Graduate School of Medicine, Nagoya, Aichi, Japan, **2** Department of Developmental Biology, Osaka Bioscience Institute, Suita, Osaka, Japan, **3** JST, CREST, Suita, Osaka, Japan, **4** Department of Biomedical Sciences, Chubu University, Kasugai, Aichi, Japan, **5** Department of Respiratory Medicine, Nagoya University Graduate School of Medicine, Nagoya, Aichi, Japan, **6** Department of Ophthalmology, Sapporo Medical University School of Medicine, Sapporo, Hokkaido, Japan, **7** Department of Ophthalmology and Visual Science, Chiba University Graduate School of Medicine, Chiba, Chiba, Japan, **8** Department of Ophthalmology, Iwate Medical University School of Medicine, Morioka, Iwate, Japan, **9** Department of Ophthalmology, Oregon Health and Science University, Portland, Oregon, United States of America

## Abstract

*Background:* Paraneoplastic retinopathy (PR), including cancer-associated retinopathy (CAR) and melanoma-associated retinopathy (MAR), is a progressive retinal disease caused by antibodies generated against neoplasms not associated with the eye. While several autoantibodies against retinal antigens have been identified, there has been no known autoantibody reacting specifically against bipolar cell antigens in the sera of patients with PR. We previously reported that the transient receptor potential cation channel, subfamily M, member 1 (TRPM1) is specifically expressed in retinal ON bipolar cells and functions as a component of ON bipolar cell transduction channels. In addition, this and other groups have reported that human TRPM1 mutations are associated with the complete form of congenital stationary night blindness. The purpose of the current study is to investigate whether there are autoantibodies against TRPM1 in the sera of PR patients exhibiting ON bipolar cell dysfunction.

*Methodology/Principal Findings:* We performed Western blot analysis to identify an autoantibody against TRPM1 in the serum of a patient with lung CAR. The electroretinograms of this patient showed a severely reduced ON response with normal OFF response, indicating that the defect is in the signal transmission between photoreceptors and ON bipolar cells. We also investigated the sera of 26 patients with MAR for autoantibodies against TRPM1 because MAR patients are known to exhibit retinal ON bipolar cell dysfunction. Two of the patients were found to have autoantibodies against TRPM1 in their sera.

*Conclusion/Significance:* Our study reveals TRPM1 to be one of the autoantigens targeted by autoantibodies in at least some patients with CAR or MAR associated with retinal ON bipolar cell dysfunction.

**Citation:** Kondo M, Sanuki R, Ueno S, Nishizawa Y, Hashimoto N, et al. (2011) Identification of Autoantibodies against TRPM1 in Patients with Paraneoplastic Retinopathy Associated with ON Bipolar Cell Dysfunction. PLoS ONE 6(5): e19911. doi:10.1371/journal.pone.0019911

**Editor:** Steven Barnes, Dalhousie University, Canada

**Received** February 10, 2011; **Accepted** April 6, 2011; **Published** May 17, 2011

**Copyright:** © 2011 Kondo et al. This is an open-access article distributed under the terms of the Creative Commons Attribution License, which permits unrestricted use, distribution, and reproduction in any medium, provided the original author and source are credited.

**Funding:** This work was supported by CREST from the Japan Science and Technology Agency (http://www.jst.go.jp/), and a Grant-in-Aid for Scientific Research (B)(C) (#20390448, #20390087, #20592075, #20791678) from the Ministry of Education, Culture, Sports, Science and Technology (http://www.jsps.go.jp/), the Takeda Science Foundation (http://www.takeda-sci.or.jp/), The Uehara Memorial Foundation (http://www.ueharazaidan.com/), the Naito Foundation (http://www.naito-f.or.jp/), the Novartis Foundation (#20-10, http://novartisfound.or.jp/), Mochida Memorial Foundation for Medical and Pharmaceutical Research (http://www.mochida.co.jp/zaidan/), the Senri Life Science Foundation (#S-2144, http://www.senri-life.or.jp/), the Kato Memorial Bioscience Foundation (http://www.katokinen.or.jp/) and the Japan National Society for the Prevention of Blindness (http://www.nichigan.or.jp/link/situmei.jsp). A grant from the National Institute of Health (E13053), was awarded to GA. The funders had no role in study design, data collection and analysis, decision to publish, or preparation of the manuscript.

**Competing Interests:** The authors have declared that no competing interests exist.

* E-mail: furukawa@obi.or.jp (TF); kondomi@med.nagoya-u.ac.jp (MK)

These authors contributed equally to this work.

## Introduction

Paraneoplastic retinopathy (PR) is a progressive retinal disorder caused by an autoimmune mechanism and is associated with the presence of anti-retinal antibodies in the serum generated against neoplasms not associated with the eye [1–4]. The retinopathy can develop either before or after the diagnosis of a neoplasm. Patients with PR can have night blindness, photopsia, ring scotoma, attenuated retinal arteriole, and abnormal electroretinograms (ERGs). The diagnosis of PR is usually made by the identification of neoplasms and anti-retinal autoantibodies in the sera.

PR includes two subgroups: cancer-associated retinopathy (CAR) [5,6] and melanoma-associated retinopathy (MAR) [7–10]. Although CAR and MAR share similar clinical symptoms, the ERG findings

are very different. Both a- and b-waves are severely attenuated in CAR, indicating extensive photoreceptor dysfunction, whereas only the b-wave is severely reduced while the a-wave is normal in MAR, suggesting bipolar cell dysfunction [8,9]. However, it was recently reported that cancers other than melanoma can cause bipolar cell dysfunction [11,12]. Several autoantibodies against retinal antigens have been identified, but a specific antigen associated with bipolar cells has not been identified in patients with CAR and MAR [1–10].

In the current study, we identified autoantibodies against the transient receptor potential cation channel, subfamily M, member 1 (TRPM1) [13–15] in the serum of one patient with lung cancer. The ERG findings in this patient indicated a selective ON-bipolar cell dysfunction. We also investigated the sera of 26 MAR patients and found that two contained autoantibodies against TRPM1. Our results suggest that TRPM1 is one of the retinal autoantigens in at least some patients with CAR or MAR and may cause retinal ON bipolar cell dysfunction.

## Results

### Case report of CAR associated with ON bipolar cell dysfunction

A 69-year-old man visited the Nagoya University Hospital with complaints of blurred vision, photopsia and night blindness in both eyes of three months duration. At this point he was not diagnosed as suffering from any eye disease or systemic disease, including a malignant tumor, and his family history revealed no other members suffering from any eye diseases. On initial examination, his best-corrected visual acuity was 0.9 in the right eye and 0.6 in the left eye. Humphrey static perimetry revealed a severe decrease in sensitivity within the central 30 degrees of the visual field in both eyes (Fig. 1A). Dark-adaptometry of this patient showed a loss of the rod branch. The cone threshold was within normal range. Ophthalmoscopy showed a nearly normal fundus appearance except for slight hypopigmentation at the macula of the left eye, which may be due to age-related changes in the retinal pigment epithelium (Fig. 1B), but fluorescein angiography demonstrated periphlebitis of the retinal vessels (arrows, Fig. 1C). Spectral-domain optical coherence tomography (SD-OCT) showed that the morphology of the retina was normal in both eyes (Fig. 1D).

### Electrophysiological examinations

Recordings of the full-field ERGs from this patient showed that the rod responses were undetectable (Fig. 2). The rod- and cone-mixed maximal response was a negative-type with an a-wave of normal amplitude and a b-wave that was smaller than the a-wave. The a-wave of the cone response had a wide trough, and the b-wave was reduced by 40%. The amplitude of the 30-Hz flicker ERG was reduced by 50%. The photopic long-flash ERG showed severely reduced ON response and normal OFF response. These ERG findings indicated that there was a defect in the signal transmission from photoreceptors to ON bipolar cells both in both rod and cone pathways.

Based on these ophthalmological and electrophysiological tests, we suspected that this patient might have PR and referred him to an internist. The general physical examination including positron emission tomography and computed tomography revealed two abnormal masses in the right lung. Biopsy of these masses confirmed that the masses were small cell carcinomas of the lung.

### Detection of autoantibodies against TRPM1 in the serum of the CAR patient

Based on our ERG examination results, we hypothesized that the serum of this CAR patient may contain autoantibodies against TRPM1. To test this hypothesis, we examined whether or not this CAR patient's serum could recognize human TRPM1 protein by Western blot analysis. We transfected an expression plasmid containing human TRPM1 cDNA with the C-terminal 3xFlag-tag (TRPM1-3xFlag) into HEK293T cells, and carried out a Western blot analysis using whole cell extracts harvested after 48 hrs cell growth. We first confirmed that TRPM1-3xFlag was expressed by cell using Western blot analysis and an anti-Flag antibody. We detected the ~200 kDa TRPM1-3xFlag band in the cell lysates (Fig. 3A).

Next, we performed Western blot analysis on the same lysates using the serum from our CAR patient and a healthy control person. We detected immunostaining of the same size protein, which was confirmed with the anti-Flag antibody, and with CAR serum. The control serum did not present a significant band (Fig. 3B, C). This result showed the presence of autoantibodies against TRPM1 in this CAR patient's serum.

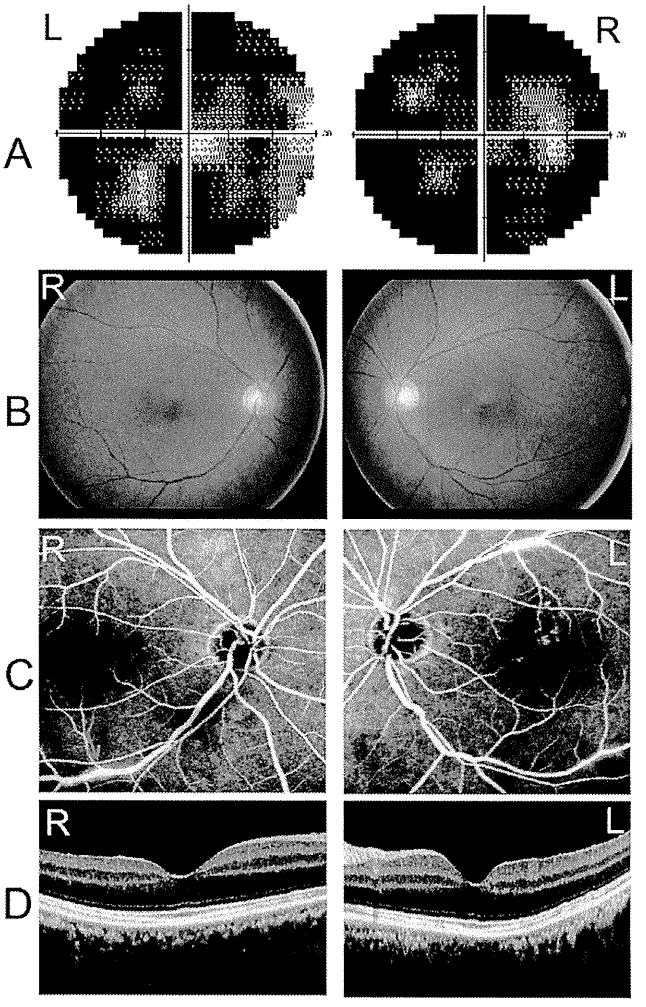


**Figure 1. Ophthalmological findings from a patient with paraneoplastic retinopathy (PR) associated with lung cancer.** (A) Threshold of static visual field (Humphrey, 30-2 program) plotted on a gray scale showing severely decreased sensitivities within the central 30 degrees of the visual field. (B) Fundus photographs of the patient showing a nearly normal fundus. (C) Fluorescein angiograms showing periphlebitis of the retinal vessels (arrows). (D) Spectral-domain optical coherence tomographic (SD-OCT) image of a 9 mm horizontal scan of the retina of our patient. The retinal structure in each retinal layer is normal.
doi:10.1371/journal.pone.0019911.g001

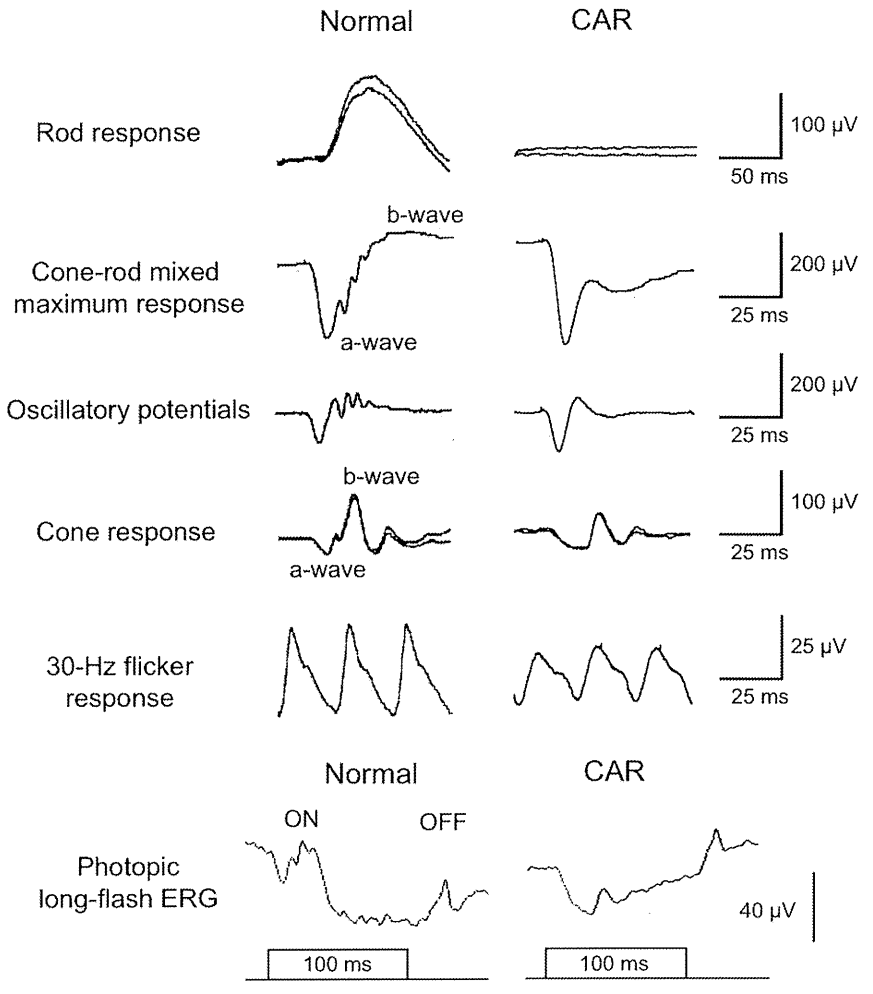


**Figure 2. Full-field ERG recordings.** The rod response was recorded with a blue light at an intensity of $5.2\times10^{-3}$ cd-s/m$^2$ after 30 minutes of dark-adaptation. The cone-rod mixed maximum response was elicited by a white flash at an intensity of 44.2 cd-s/m$^2$. The oscillatory potentials were recorded with a white flash at an intensity of 44.2 cd-s/m$^2$ using a band-pass filter of 50–1000 Hz. The cone response and a 30 Hz flicker response were elicited by a white stimulus of 4 cd-s/m$^2$ and 0.9 cd-s/m$^2$, respectively, on a blue background of 30 cd/m$^2$. Photopic long-flash ERG responses were also elicited by long-duration flashes of 100 ms using a densely-packed array of white LEDs of 200 cd/m$^2$ on a white background of 30 cd/m$^2$. doi:10.1371/journal.pone.0019911.g002

To examine whether the serum from the CAR patient recognized retinal bipolar cells, we carried out an immunohistochemical analysis on monkey and mouse retinas. We first performed immunohistochemistry on the retina of a 3-year-old rhesus monkey (*Macaca mulata*) and on the retina of a one-month-old C57/B6 mouse using the serum of the CAR patient, however, we did not obtain a significant staining signal above background (data not shown). We then concentrated the serum by IgG purification followed by filter spin column centrifugation and performed immunohistochemistry on the monkey retina using the concentrated serum (Fig. 3D–G). We observed a significant immunolabeling on the INL in the monkey retina (Fig. 3D, F) whereas the normal serum did not give a significant labeling (Fig. 3E, G). The antibodies immuolabeled both the bipolar side and amacrine side of the INL. Since most of the cells residing on the outer side of the INL are ON bipolar cells, at least some of the stained cells are ON bipolar cells. It should be noted some of the staining signals show a spotted pattern in the outer plexiform layer (Fig. 3F) as is observed in TRPM1 or mGluR6 immunostaining on the mouse retina [13], suggesting that the CAR patient serum recognizes the bipolar dendritic tips where some of the TRPM1 protein localizes.

## Western blot analysis of the sera from MAR patients

Since the functional defect in the retina of MAR patients is known to be due to abnormal signal transmission between photoreceptors and ON bipolar cells [8,9], we then investigated whether or not autoantibodies to TRPM1 were also present in the sera of MAR patients. We obtained the sera of 26 MAR patients from two hospitals in Japan (Chiba University Hospital and Iwate Medical University Hospital) and Ocular Immunology Laboratory in the USA (Casey Eye Institute). We found that the sera from patients #8 and #23 exhibited a significant immunoreactive band against TRPM1-transfected cell lysates by Western blot analysis (Fig. 4A and B). The control serum showed no significant immune response against the TRPM1-transfected cell lysates (Fig. 3C). These results suggest that the sera from some MAR patients contain autoantibodies against TRPM1. Due to the limited volume of sera from the MAR patients, we could not try immunostaining on the monkey or the mouse retina using the serum from the patients #8 and #23.

MAR patient #8, was a 76-year-old man with a history of skin melanoma. He had ring scotomas and abnormal ERGs indicating that he had MAR. The other patient, MAR #23, was a 57-year-

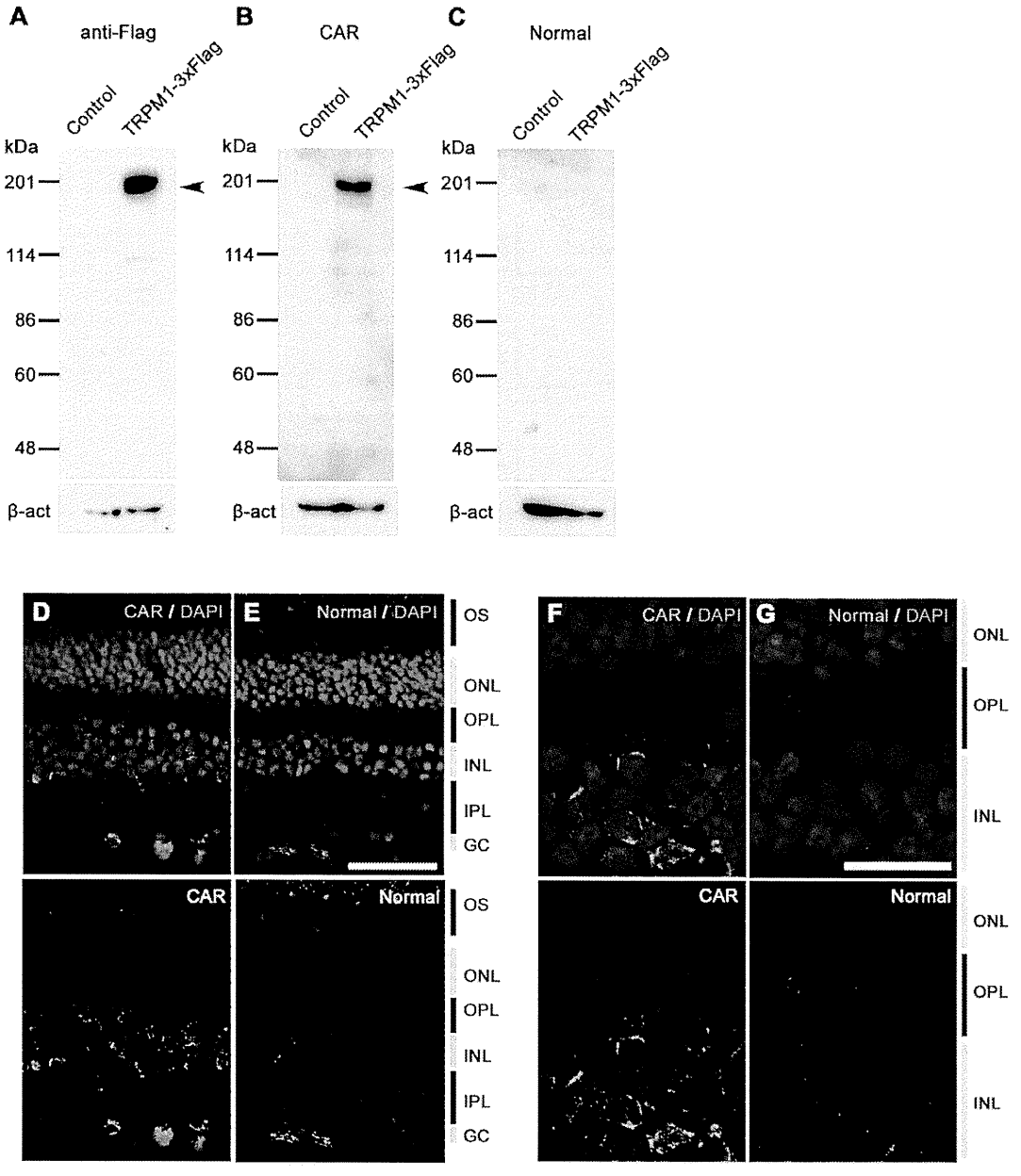


**Figure 3. Immunostaining and Western blot analysis of human TRPM1 using serum from the CAR patient.** (A–C) Immunoblots of the transfected cell lysates using an antibody against Flag tag (A), serum from CAR patient (B), and control serum (C). Arrowheads indicate the TRPM1-3xFlag protein bands. HEK293T cells were transfected with the pCAGGS or pCAGGS-human TRPM1-3xFlag plasmid, and cells were harvested after 48 hrs. β-actin (β-act) was used for a loading control. (D–G) Confocal images of a three-year-old rhesus monkey retina immunostained with the concentrated serum from the CAR patient (D, F) or the concentrated normal serum (E, G). Cell nuclei are visualized with DAPI. CAR patient serum presented signals on INL cells and the inner part of the OPL (D, F). Scale bar = 50 μm in (E) and 20 μm in (G).
doi:10.1371/journal.pone.0019911.g003

old man with poor night vision, abnormal scotopic ERGs and abnormal color vision. He had a history of skin melanoma and thyroid cancer. There was no other clinical information available on these two patients because these sera were obtained from other institutes several years before without detailed clinical information.

## Discussion

PR, including MAR and CAR, presents visual disorders associated with systemic cancer. Antibodies against retinal cells and proteins have been detected in the sera of patients with PR suggesting an autoimmune basis for the etiology of the PR. The autoantibodies identified so far include rhodopsin, retinal transducin alpha and beta, recoverin, S-arrestin, α-enolase, carbonic anhydrase II, and heat shock protein-60 which reside abundantly in photoreceptors [1–10,16]. MAR and CAR can cause bipolar cell dysfunction [7–12]. The results of the ERG [8,9] and immunohistochemistry [7] studies suggested that the main target of MAR are retinal ON bipolar cells in both the rod and cone pathways. However, autoantibodies specifically reacting with a bipolar cell antigen had not been identified in the sera of patients with PR, including those with CAR and MAR. In the current study, we identified autoantibodies against TRPM1, a component of the ON bipolar cell transduction channel negatively regulated by Goα in the mGluR6 signaling pathway [13–15], in the

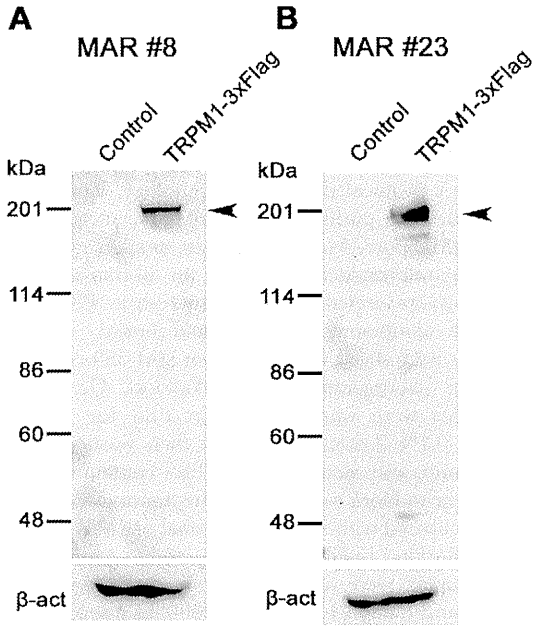


**Figure 4. Western blot analysis of human TRPM1 using sera from the MAR patients.** (A, B) Immunoblots of the transfected cell lysates using sera from MAR patient #8 (A) and MAR patient #23 (B). HEK293T cells were transfected with pCAGGS or pCAGGS-human TRPM1-3xFlag plasmid, and cells were harvested after 48 hrs. Arrowheads indicate the TRPM1-3xFlag protein bands. β-actin (β-act) was used for a loading control.
doi:10.1371/journal.pone.0019911.g004

sera of one CAR patient and two MAR patients. The CAR patient exhibited a dysfunction of ON bipolar cells, and to our knowledge, this is the first report on an autoantibody against a bipolar cell antigen in the serum of PR patients affecting the ON bipolar cell function.

Previously, we isolated a mouse *TRPM1-L* cDNA corresponding to the human long form of *TRPM1*, and found that the TRPM1-L protein is developmentally localized at the tips of the ON bipolar dendrites co-localizing with mGluR6, but not on OFF bipolar cells [13,14]. The *TRPM1* null mutant mouse completely loses the ON bipolar cell photoresponses to light, indicating that TRPM1 plays a critical role in the synaptic transmission from photoreceptors to ON-bipolar cells [13,15]. In addition, we demonstrated using a CHO cell reconstitution system that TRPM1-L is a nonselective cation channel which is negatively regulated by Goα downstream of the mGluR6 signaling cascade in ON bipolar cells [13]. Recently, four groups including ours independently reported that mutations of human *TRPM1* are associated with the complete-type of congenital stationary night blindness (cCSNB), an inherited human retinal disease [17–20]. cCSNB is a non-progressive retinal disease characterized by congenital night blindness with a moderate decrease in visual acuity and myopia [21-24]. Previous ERG studies have suggested that the defect in cCSNB patients lies in the signal transmission from photoreceptors to ON bipolar cells in both the rod and cone pathways [25–28]. We have identified five different mutations in our three cCSNB patients, and have shown that these mutations lead to either abnormal TRPM1 protein production or mislocalization of the TRPM1 protein in bipolar cell dendrites [17]. These results suggest that TRPM1 plays a critical role in mediating the photoresponses of ON bipolar cells in humans as well. Based on these findings, we hypothesize that the ectopic expression of TRPM1 in tumor cells of some CAR and MAR patients may result in aberrant production of autoantibodies to TRPM1 through B-lymphocytic responses [29–32]. These antibodies may react to the TRPM1 protein in retinal ON bipolar cells resulting in dysfunction of the TRPM1 transduction cation channel downstream of the mGluR6 signaling cascade. However, we could not confirm whether TRPM1 is expressed in the tumor cells of the three PR patients examined in this study [29] because tumor samples were not available.

Another question regarding the disease mechanism underlying PR is whether the binding of TRPM1 autoantibody to bipolar cells results in the cell death or dysfunction of bipolar cells. As far as we examined the retinal structure of the CAR patient using a spectral domain optical coherence tomography (SD-OCT) retinal imaging device, the structure of the retinal bipolar cell layer appeared to be well preserved even three months after the onset of symptoms (Fig.1D). This suggests that the autoantibodies reacting to TRPM1 cause dysfunction of the ON bipolar transduction pathway rather than bipolar cell death. However, further studies are needed to clarify the exact disease mechanism.

In the sera of MAR patients, several types of autoantibodies against retinal proteins have been reported, including the 22 kDa neuronal antigen GNB1, rhodopsin, S-arrestin, and aldolase-A and -C [10,16,33,34]. We initially considered that TRPM1 might be a major MAR target antigen, because TRPM1 is exclusively expressed in retinal ON bipolar cells. However, autoantibodies against TRPM1 were detected in only two out of 26 MAR. patients' sera (7.7%, Fig. 4A, B). We tested whether the sera of one CAR patient and 26 MAR patients recognized human mGluR6, which is specifically expressed in ON bipolar cells, however, none of the sera exhibited a significant band in Western blot analysis (data not shown). Thus, antigens other than TRPM1 or mGluR6 may be involved in the pathogenesis of a large proportion of MAR.

Immunohistochemical analyses using the serum of the CAR patient showed labeling in the inner nuclear layer and outer plexiform layer of the adult rhesus monkey retina (Fig. 3D–G), where the bipolar cell bodies and dendrites reside, respectively. This immunostaining pattern is somewhat similar to our previous immunostaining results on the mouse retina with specific antibody against mouse TRPM1-L, which corresponds to the human TRPM1 long form [13]. Other labeling was also observed in the amacrine cells and ganglion cells. The reason for the immunoreactivity with these cells is uncertain, however, it may be due to the presence of other autoantibodies against amacrine cell and ganglion cell antigens. Lu *et al.* reported the presence of various different autoantibodies in the serum of a single PR patient [10]. If this is the case, it may explain why our CAR patient displayed severely reduced visual sensitivities in the visual field tests (Fig. 1A) unlike cCSNB patients with TRPM1 mutations[17].

It should be noted that we did not confirm whether there are any antoantibodies against TRPM1 in the sera of normal subjects by using a large number of samples. However, this possibility is thought to be low, because Shimazaki *et al.* reported that the molecular weights of the IgGs with observed anti-retinal reactivity in 92 normal sera were smaller than 148 kDa, which is smaller than the TRPM1 molecular weight of ~200 kDa, although relatively high molecular weight reactivity was not intensively investigated [35].

One limitation of the current study is that we could not obtain detailed information on the two MAR patients, MAR #8 and #23, associated with the TRPM1 autoantibody. We confirmed that these two patients had skin melanomas accompanying the visual disturbances, but could not obtain a more detailed clinical history or data on visual acuity, visual field, or ERGs because these sera were sent from different hospitals several years ago. Thus, we do not know whether these two MAR patients really had retinal ON bipolar cell dysfunction. Further prospective studies of the TRPM1 autoantibodies in large numbers of MAR patients are needed.

In conclusion, our study suggests that TRPM1 may be one of the causative antigens responsible for PR associated with ON bipolar cell dysfunction.

### Note added in proof

During the course of revision process of this manuscript, Dhingra *et al.* (J. Neurosci. 31, 3962–3967, 2011) independently reported the presence of autoantibodies against TRPM1 in two MAR patients. Our study reports on autoantibodies against TRPM1 in CAR serum in addition to MAR sera.

## Materials and Methods

### Subjects

The Nagoya University Hospital Ethics Review Board approved this study (approval ID 1131). Of the PR patients that were examined in the Nagoya University Hospital, one PR patient with lung cancer and ON bipolar cell dysfunction was studied in detail. The examinations included routine ophthalmological and electrophysiological tests. In addition, immunohistochemical and Western blot analyses were performed using the serum of this patient. The procedures used conformed to the tenets of the Declaration of Helsinki of the World Medical Association. A written informed consent was obtained from the patient after he was provided with sufficient information on the procedures to be used.

We also obtained sera of 26 patients with MAR from two hospitals in Japan (Chiba University Hospital and Iwate Medical University Hospital) and Ocular Immunology Laboratory in the USA (Casey Eye Institute) for Western blot analysis.

### Ophthalmologic examinations

The ophthalmologic examination included best-corrected visual acuity, biomicroscopy, ophthalmoscopy, fundus photography, fluorescein angiography, static perimetry, and spectral-domain optical coherence tomography (SD-OCT). Static visual fields were obtained with the Humphrey 30-2 program (Carl Zeiss, Dublin, USA), and the results are shown in gray scale. SD-OCT was performed with a 9-mm horizontal scan through the midline with 50 averages (Spectralis HRA+OCT; Heidelberg Engineering, Vista, CA).

### Electroretinograms (ERG)

Full-field ERGs were elicited with a Ganzfeld dome and recorded with a Burian-Allen bipolar contact lens electrode. The ground electrode was attached to the ipsilateral ear.

After 30 minutes of dark-adaptation, a rod response was elicited with a blue light at an intensity of $5.2\times10^{-3}$ cd-s/m$^2$. A cone-rod mixed maximum response was elicited by a white flash at an intensity of 44.2 cd-s/m$^2$. A cone response and a 30 Hz flicker response were elicited by a white stimulus of 4 cd-s/m$^2$ and 0.9 cd-s/m$^2$, respectively, on a blue background of 30 cd/m$^2$. Full-field cone ERGs were also elicited by long-duration flashes of 100 ms using a densely packed array of white LEDs. The array was positioned at the top of the Ganzfeld dome and covered by a diffuser. The stimulus intensity and background illumination measured in the dome was 200 cd/m$^2$ and 30 cd/m$^2$, respectively. Responses were amplified by 10K and the band pass was set to 0.3 to 1000 Hz. The data were digitized at 4.3 kHz, and 5 to 20 responses were averaged (Neuropack, Nihonkohden, Tokyo, Japan).

### Immunohistochemistry

For immunohistochemistry, patient and normal sera (300 µl) were purified using the Melon Gel IgG purification kit according to the manufacturer's protocol (Pierce Biotechnology, Rockford, IL) to remove IgM, and purified sera were concentrated by Amicon Ultra 100 (Millipore, MA). The rhesus monkey eye cup was fixed with 4% paraformaldehyde in PBS for 30 min at 4°C. The samples were cryoprotected with 30% sucrose in PBS and embedded in OCT compound (Sakura Finetechnical, Tokyo, Japan). These tissues were sliced with a Microm HM 560 cryostat microtome (Microm Laborgeräte GmbH, Walldorf, Germany) into 14 µm. Sections were washed twice in PBS for 5 min, permeabilized with 0.1% Triton-X100/PBS, then washed with PBS 3 times for 5 min, and incubated with PBS containing 4% donkey serum for 1 hr to block samples. For the immunoreaction, the samples were incubated with a purified normal or CAR serum (1:300) diluted in blocking buffer at 4°C overnight. After PBS-washing, these samples were incubated with a DyLight-488 conjugated donkey anti-human IgG (H+L) (1:400) as a secondary antibody (Jackson Immunoresearch Laboratories) at room temperature for 1 hr and washed with PBS.

### Transfection and Western blot analyses

HEK293T cells were cultured in D-MEM containing 10% fetal bovine serum (FBS; Nissui, Tokyo, Japan). These cells were grown under 5% carbon dioxide at 37°C. The calcium phosphate method was used to transfect the cells. Transfected cells were incubated at 37°C for 48 hrs, and then harvested for further analysis. The proteins extracted from the cells were separated by SDS–PAGE on a 7.5% precast gel (ATTO, Tokyo, Japan), and then transferred to a polyvinylidene difluoride membrane using the Invitrogen iBlot system (Invitrogen, Carlsbad, CA, USA). The membrane was incubated with primary antibodies, mouse anti-Flag (1:1,000; Sigma, St Louis, MO), sera from patients (1:100), normal human serum (1:100), or mouse anti-β-actin (1:5,000; Sigma). The membrane was then incubated with a horseradish peroxidase-conjugated goat anti-mouse IgG (1:10,000; Zymed Laboratories, San Francisco, CA) or donkey anti-human IgG (1:10,000; Jackson Immuno Research Laboratories, West Grove, PA) as secondary antibodies. The bands were developed using Chemi-Lumi One L (Nacalai Tesque, Kyoto, Japan).

## Acknowledgments

We thank Richaed G. Weleber, Yozo Miyake, and Duco I. Hamasaki for helpful discussions of this study, Junko Hanaya for collecting the serum of our patients, and Mikiko Kadowaki, Aiko Ishimaru, Kaori Sone, and Shawna Kennedy for technical assistance.

## Author Contributions

Conceived and designed the experiments: MK TF. Performed the experiments: MK RS SU YN NH. Analyzed the data: MK RS SU TF. Contributed reagents/materials/analysis tools: MK SU HO SY SM HT GA. Wrote the paper: MK TF. Supervised the project: MK HT TF.

## References

1. Thirkill CE, FitzGerald P, Sergott RC, Roth AM, Tyler NK, et al. (1989) Cancer-associated retinopathy (CAR syndrome) with antibodies reacting with retinal, optic-nerve, and cancer cells. N Engl J Med 321: 1589–1594.
2. Chan JW (2003) Paraneoplastic retinopathies and optic neuropathies. Surv Ophthalmol 48: 12–38.
3. Heckenlively JR, Ferreyra HA (2008) Autoimmune retinopathy: A review and summary. Semin Immunopathol 30: 127–134.
4. Adamus G (2009) Autoantibody targets and their cancer relationship in the pathogenicity of paraneoplastic retinopathy. Autoimmun Rev 8: 410–414.

5. Thirkill CE, Roth AM, Keltner JL (1987) Cancer-associated retinopathy. Arch Ophthalmol 105: 372–375.
6. Jacobson DM, Thirkill CE, Tipping SJ (1990) A clinical triad to diagnose paraneoplastic retinopathy. Ann Neurol 28: 162–167.
7. Milam AH, Saari JC, Jacobson SG, Lubinski WP, Feun LG, et al. (1993) Autoantibodies against retinal bipolar cells in cutaneous melanoma-associated retinopathy. Invest Ophthalmol Vis Sci 34: 91–100.
8. Alexander KR, Fishman GA, Peachey NS, Marchese AL, Tso MOM (1992) "On" response defect in paraneoplastic night blindness with cutaneous malignant melanoma. Invest Ophthalmol Vis Sci 33: 477–483.
9. Lei B, Bush RA, Milam AH, Sieving PA (2000) Human melanoma-associated retinopathy (MAR) antibodies alter the retinal ON-response of the monkey ERG in vivo. Invest Ophthalmol Vis Sci 41: 262–266.
10. Lu Y, Jia L, He S, Hurley MC, Leys MJ, et al. (2009) Melanoma-associated retinopathy: a paraneoplastic autoimmune complication. Arch Ophthalmol 127: 1572–1580.
11. Jacobson DM, Adamus G (2001) Retinal anti-bipolar cell antibodies in a patient with paraneoplastic retinopathy and colon carcinoma. Am J Ophthalmol 131: 806–808.
12. Goetgebuer G, Kestelyn-Stevens AM, De Laey JJ, Kestelyn P, Leroy BP (2008) Cancer-associated retinopathy (CAR) with electronegative ERG: a case report. Doc Ophthalmol 116: 49–55.
13. Koike C, Obara T, Uriu Y, Numata T, Sanuki R, et al. (2010) TRPM1 is a component of the retinal ON bipolar cell transduction channel in the mGluR6 cascade. Proc Natl Acad Sci U S A 107: 332–337. Epub Dec. 4, 2009.
14. Koike C, Numata T, Ueda H, Mori Y, Furukawa T (2010) TRPM1: A vertebrate TRP channel responsible for retinal ON bipolar function. Cell Calcium 48: 95–101.
15. Morgans CW, Zhang J, Jeffrey BG, Nelson SM, Burke NS, et al. (2009) TRPM1 is required for the depolarizing light response in retinal ON-bipolar cells. Proc Natl Acad Sci U S A 106: 19174–19178.
16. Hartmann TB, Bazhin AV, Schadendorf D, Eichmüller SB (2005) SEREX identification of new tumor antigens linked to melanoma-associated retinopathy. Int J Cancer 114: 88–93.
17. Nakamura M, Sanuki R, Yasuma TR, Onishi A, Nishiguchi KM, et al. (2010) TRPM1 mutations are associated with the complete form of congenital stationary night blindness. Mol Vis 16: 425–437.
18. Li Z, Sergouniotis PI, Michaelides M, Mackay DS, Wright GA, et al. (2009) Recessive mutations of the gene TRPM1 abrogate ON bipolar cell function and cause complete congenital stationary night blindness in humans. Am J Hum Genet 85: 711–719.
19. van Genderen MM, Bijveld MM, Claassen YB, Florijn RJ, Pearring JN, et al. (2009) Mutations in TRPM1 are a common cause of complete congenital stationary night blindness. Am J Hum Genet 85: 730–736.
20. Audo I, Kohl S, Leroy BP, Munier FL, Guillonneau X, et al. (2009) TRPM1 is mutated in patients with autosomal-recessive complete congenital stationary night blindness. Am J Hum Genet 85: 720–729.
21. Miyake Y, Yagasaki K, Horiguchi M, Kawase Y, Kanda T (1986) Congenital stationary night blindness with negative electroretinogram: A new classification. Arch Ophthalmol 104: 1013–1020.
22. Bech-Hansen NT, Naylor MJ, Maybaum TA, Sparkes RL, Koop B, et al. (2000) Mutations in NYX, encoding the leucine-rich proteoglycan nyctalopin, cause X-linked complete congenital stationary night blindness. Nat Genet 26: 319–23.
23. Pusch CM, Zeitz C, Brandau O, Pesch K, Achatz H, et al. (2000) The complete form of X-linked congenital stationary night blindness is caused by mutations in a gene encoding a leucine-rich repeat protein. Nat Genet 26: 324–327.
24. Dryja TP, McGee TL, Berson EL, Fishman GA, Sandberg MA, et al. (2005) Night blindness and abnormal cone electroretinogram ON responses in patients with mutations in the GRM6 gene encoding mGluR6. Proc Natl Acad Sci USA 102: 4884–4889.
25. Miyake Y, Yagasaki K, Horiguchi M, Kawase Y (1987) On- and off-responses in photopic electroretinogram in complete and incomplete types of congenital stationary night blindness. Jpn J Ophthalmol 31: 81–87.
26. Houchin K, Purple RL, Wirtschafter JD (1991) X-linked congenital stationary night blindness and depolarizing bipolar system dysfunction. [ARVO abstract]. Invest Ophthalml Vis Sci 32: S1229.
27. Young RSL (1991) Low-frequency component of the photopic ERG in patients with X-linked congenital stationary night blindness. Clin Vis Sci 6: 309–315.
28. Khan NW, Kondo M, Hiriyanna KT, Jamison JA, Bush RA, et al. (2005) Primate retinal signaling pathways: Suppressing ON-pathway activity in monkey with glutamate analogues mimics human CSNB1-NYX genetic night blindness. J Neurophysiol 93: 481–492.
29. Polans AS, Witkowska D, Haley TL, Amundson D, Baizer L, et al. (1995) Recoverin, a photoreceptor-specific calcium-binding protein, is expressed by the tumor of a patient with cancer-associated retinopathy. Proc Natl Acad Sci U S A 92: 9176–9180.
30. Matsubara S, Yamaji Y, Sato M, Fujita J, Takahara J (1996) Expression of a photoreceptor protein, recoverin, as a cancer-associated retinopathy autoantigen in human lung cancer cell lines. Br J Cancer 74: 1419–1422.
31. Ohguro H, Odagiri H, Miyagawa Y, Ohguro I, Sasaki M, et al. (2004) Clinicopathological features of gastric cancer cases and aberrantly expressed recoverin. Tohoku J Exp Med 202: 213–219.
32. Bazhin AV, Schadendorf D, Willner N, De Smet C, Heinzelmann A, et al. (2007) Photoreceptor proteins as cancer-retina antigens. Int J Cancer 120: 1268–76.
33. Keltner JL, Thirkill CE (1999) The 22-kDa antigen in optic nerve and retinal diseases. J Neuroophthalmol 19: 71–83.
34. Potter MJ, Adamus G, Szabo SM, Lee R, Mohaseb K, et al. (2002) Autoantibodies to transducin in a patient with melanoma-associated retinopathy. Am J Ophthalmol 134: 128–30.
35. Shimazaki K, Jirawuthiworavong GV, Heckenlively JR, Gordon LK (2008) Frequency of anti-retinal antibodies in normal human serum. J Neuro-Ophthalmol 28: 5–11.

# miR-124a is required for hippocampal axogenesis and retinal cone survival through Lhx2 suppression

Rikako Sanuki[1,2], Akishi Onishi[1,2], Chieko Koike[1], Rieko Muramatsu[3], Satoshi Watanabe[1,2], Yuki Muranishi[1], Shoichi Irie[1,2], Shinji Uneo[4], Toshiyuki Koyasu[4], Ryosuke Matsui[5], Yoan Chérasse[6], Yoshihiro Urade[6], Dai Watanabe[5], Mineo Kondo[4], Toshihide Yamashita[3] & Takahisa Furukawa[1,2]

**MicroRNA-124a (miR-124a) is the most abundant microRNA expressed in the vertebrate CNS. Despite past investigations into the role of miR-124a, inconsistent results have left the *in vivo* function of miR-124a unclear. We examined the *in vivo* function of miR-124a by targeted disruption of *Rncr3* (*retinal non-coding RNA 3*), the dominant source of miR-124a. *Rncr3*$^{-/-}$ mice exhibited abnormalities in the CNS, including small brain size, axonal mis-sprouting of dentate gyrus granule cells and retinal cone cell death. We found that *Lhx2* is an *in vivo* target mRNA of miR-124a. We also observed that LHX2 downregulation by miR-124a is required for the prevention of apoptosis in the developing retina and proper axonal development of hippocampal neurons. These results suggest that miR-124a is essential for the maturation and survival of dentate gyrus neurons and retinal cones, as it represses *Lhx2* translation.**

© 2011 Nature America, Inc. All rights reserved.

MicroRNAs (miRNAs) are small RNAs that regulate gene expression by base-pairing to mRNAs. Notably, miR-124a is completely conserved at the nucleotide level from worms to humans and is estimated to be the most abundant miRNA in the brain, accounting for 25–48% of all brain miRNAs[1]. In addition, the human miR-124a-1 locus is located in the chromosome 8p23 region, which is rich in genes that have been implicated in neuropsychiatric disorders, microcephaly and epilepsy[2]. Overexpression of miR-124a in HeLa cells leads to the suppression of a large number of non-neuronal transcripts[3]. Moreover, a neurogenesis suppressor gene, *Ctdsp1*, and a neuron-specific splicing repressor gene, *Ptbp1*, have been identified as miR-124a target genes *in vitro*[4,5], and an increase of *Ptbp1* mRNA was observed in the telencephalon of a *Dicer* conditional knockout mouse[5]. *In vivo* knockdown of miR-124a in mouse SVZ cells identified *Sox9*, a neurogenesis suppressor gene, as a miR-124a target, suggesting that miR-124a controls neurogenesis through suppression of *Sox9* translation[6]. One study found that miR-124a is required for neuronal determination in the developing chick neural tube[4]. On the other hand, another study reported that miR-124a is not involved in the initial neuronal differentiation in the developing chick spinal cord[7]. A *Dicer* conditional knockout mice exhibited initial neurogenesis in the absence of miRNA production[8,9]. Considering these inconsistent observations, the target genes of miR-124a and its functional role in neural differentiation remain ambiguous.

## RESULTS

### *Rncr3* is the dominant source of miR-124a

Previously, we used a screen to identify functionally important molecules in the retina[10] and isolated mouse *Rncr3* cDNA[11], which is highly expressed in the retina. We examined the expression profiles of *Rncr3* by northern blot analysis and detected a ~4.1-kb full-length *Rncr3* band specifically in the CNS tissues (**Fig. 1a**). We identified a stem loop of precursor miR-124a-1 (pre-miR-124a-1), which is encoded in exon of *Rncr3*. *Rncr3* fulfilled certain criteria for being a miR-124a precursor, including high expression in the brain, nuclear localization and the presence of a consensus sequence[12] (data not shown). We examined the expression patterns of *pre-miR-124a* and *miR-124a* and confirmed that they were specifically expressed in the CNS, including the retina (**Fig. 1b**). We then investigated the localization of *Rncr3* and miR-124a in the developing retina and brain using *in situ* hybridization (**Fig. 1c–i**). Both *Rncr3* and miR-124a signals were strongly detected in ganglion cells and differentiating neurons at embryonic day 13.5 (E13.5; **Fig. 1c,f**), and those signals gradually increased until the mice were 1 month old (**Fig. 1d,e,g,h**). The abundant miR-124a signals in photoreceptor cells accumulated in the inner segment from postnatal day 1 (P1) to adulthood (1 month of age; **Fig. 1g,h**). In the adult mice, the miR-124a signal was detected in differentiated neurons, except for putative Müller glial cells in the inner nuclear layer (**Fig. 1e,h**), consistent with previous findings[13]. In the P6 brain, *Rncr3* RNA was broadly expressed, especially in the hippocampus and the upper third of the cortex (**Fig. 1i**). These results suggest that *Rncr3* is specifically expressed in the CNS and functions as a primary miR-124a-1 (pri-miR-124a-1).

To determine the function of miR-124a *in vivo*, we generated *Rncr3*$^{-/-}$ mice by replacing all of the exons of *Rncr3* with the *PGK-neo* cassette (**Fig. 2a–c**). *Rncr3*$^{-/-}$ mice were initially viable and appeared to be normal; however, about two-thirds of the *Rncr3*$^{-/-}$ mice gradually

[1]Department of Developmental Biology, Osaka Bioscience Institute, Suita, Osaka, Japan. [2]Japan Science and Technology Agency (JST), Core Research for Evolutional Science and Technology (CREST), Osaka Bioscience Institute, Suita, Osaka, Japan. [3]Department of Molecular Neuroscience, Graduate School of Medicine, Osaka University, Suita, Osaka, Japan. [4]Department of Ophthalmology, Nagoya University Graduate School of Medicine, Showa-ku, Nagoya, Japan. [5]Department of Biological Sciences, Faculty of Medicine, Graduate School of Biostudies, Kyoto University, Yoshida, Sakyo-ku, Kyoto, Japan. [6]Department of Molecular Behavioral Biology, Osaka Bioscience Institute, Suita, Osaka, Japan. Correspondence should be addressed to T.F. (furukawa@obi.or.jp).

Received 2 May; accepted 30 June; published online 21 August 2011; doi:10.1038/nn.2897

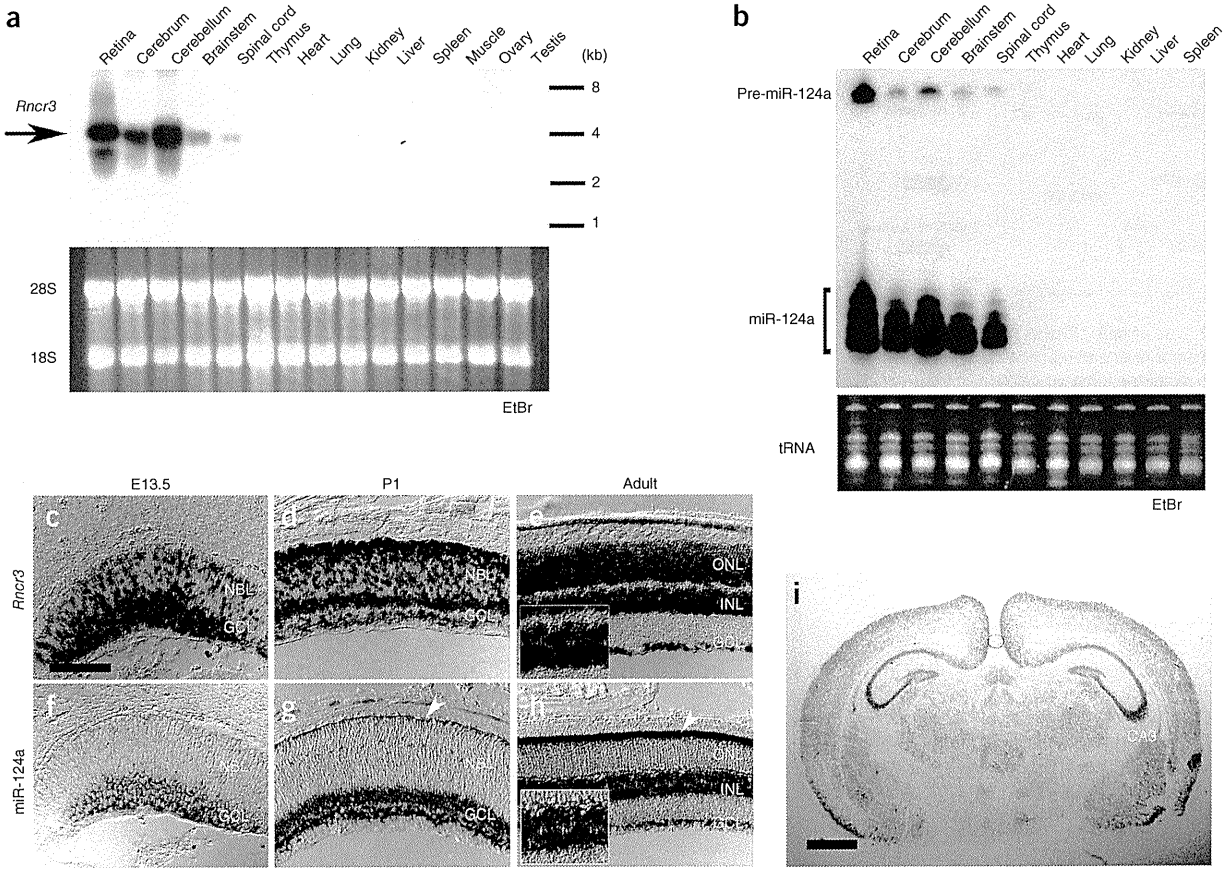


**Figure 1** Expression of *Rncr3* and miR-124a. (**a**) Northern blot analysis of *Rncr3* transcripts in adult mouse tissues. The arrow indicates the approximately 4.1-kb *Rncr3* full-length mRNA. The lower panel shows ethidium bromide (EtBr) staining of RNA. (**b**) Northern blot analysis of miR-124a in adult mouse tissues. The upper panel shows miR-124a signals obtained from LNA-modified anti–miR-124a probe. The lower panel shows EtBr staining of small RNA. (**c–h**) Expression of *Rncr3* (**c–e**) and miR-124a (**f–h**) was detected by *in situ* hybridization in the developing retina at E13.5 (**c,f**), P1 (**d,g**) and in adult mice (1 month old, **e,h**). miR-124a signal was detected in the developing photoreceptor layer at P1 and the inner segments of photoreceptors in adults (**g** and **h**, arrowheads). The small boxes in **e** and **h** show unstained blank spots by *in situ* hybridization, which may correspond to Müller glia cells in the inner nuclear layer (INL). Scale bar represents 100 μm. (**i**) Expression of *Rncr3* in the developing brain at P6. Scale bar represents 1 mm. CTX, cortex; DG, dentate gyrus; GCL, ganglion cell layer; NBL, neuroblastic layer; ONL, outer nuclear layer.

© 2011 Nature America, Inc. All rights reserved.

became debilitated and died around P20 for unknown reasons. We compared miR-124a expression among wild-type, *Rncr3*$^{+/-}$ and *Rncr3*$^{-/-}$ mice and found that miR-124a band intensities were substantially reduced by 60–80% in all of the *Rncr3*$^{-/-}$ CNS regions that we examined at P14 (**Fig. 2d**). We then performed northern blots for miR-124a and an absolute quantitative RT-PCR (qPCR) assay for pri-miR-124a-1, pri-miR-124a-2 and pri-miR-124a-3 using the retina, hippocampus and cortex of P6 wild-type and *Rncr3*$^{-/-}$ mice (**Supplementary Fig. 1**). miR-124a expression was reduced by 60–80% in *Rncr3*$^{-/-}$ mice (**Supplementary Fig. 1a**) and pri-miR-124a-3 was undetectable in both wild-type and *Rncr3*$^{-/-}$ mice (**Supplementary Fig. 1b**), indicating that *Rncr3* (pri-miR-124a-1) is the dominant source of miR-124a.

We then examined the tissue distribution of miR-124a in developing *Rncr3*$^{-/-}$ mice using *in situ* hybridization to identify tissues in which miR-124a knockout was not compensated for by expression of pre-miR-124a-2 or pre-miR-124a-3. miR-124a expression was substantially reduced and barely detectable in the presumptive photoreceptor layer (PPL), where cone photoreceptor neurogenesis occurs from E11 to E18 (refs. 14,15), of *Rncr3*$^{-/-}$ retina at E15.5 (**Fig. 2e–h**), whereas NEUROD1, a neuronal differentiation and early photoreceptor marker, was detected at normal levels (wild type, 908.5 ± 58.2 cells per section; *Rncr3*$^{-/-}$, 919 ± 33.8; $P = 0.79$; **Fig. 2i–l**). In the E17.5 wild-type retina, pri-miR-124a-1 (*Rncr3*) was strongly observed in the PPL; however, the pri-miR-124a-2 host gene was barely expressed and pri-miR-124a-3 was undetectable (**Supplementary Fig. 2a–f**), suggesting that pri-miR124a-1 is the predominant source of miR-124a in the PPL.

We next observed sections of the P6 developing *Rncr3*$^{-/-}$ brain (**Fig. 2m–p**). The *Rncr3*$^{-/-}$ brain was smaller than that of the wild type, but its morphology was not substantially affected (**Fig. 2m,n**). miR-124a expression was significantly reduced in the *Rncr3*$^{-/-}$ brain compared with that in the wild-type brain, as determined by *in situ* hybridization (**Fig. 2o,p**). We found an especially substantial loss of miR-124a expression in the *Rncr3*$^{-/-}$ hippocampal dentate gyrus (**Fig. 2p**). Our results suggest that miR-124a expression is almost abolished in the developing cone photoreceptor layer and dentate gyrus in the hippocampus. Thus, we focused our analysis on retinal cone photoreceptors and the dentate gyrus.

### *Rncr3*$^{-/-}$ mice exhibit neuronal dysfunction and dysmaturation

We first analyzed cone cells in the *Rncr3*$^{-/-}$ retina. We performed flat-mount immunostaining using 2-month-old *Rncr3*$^{-/-}$ retinas and

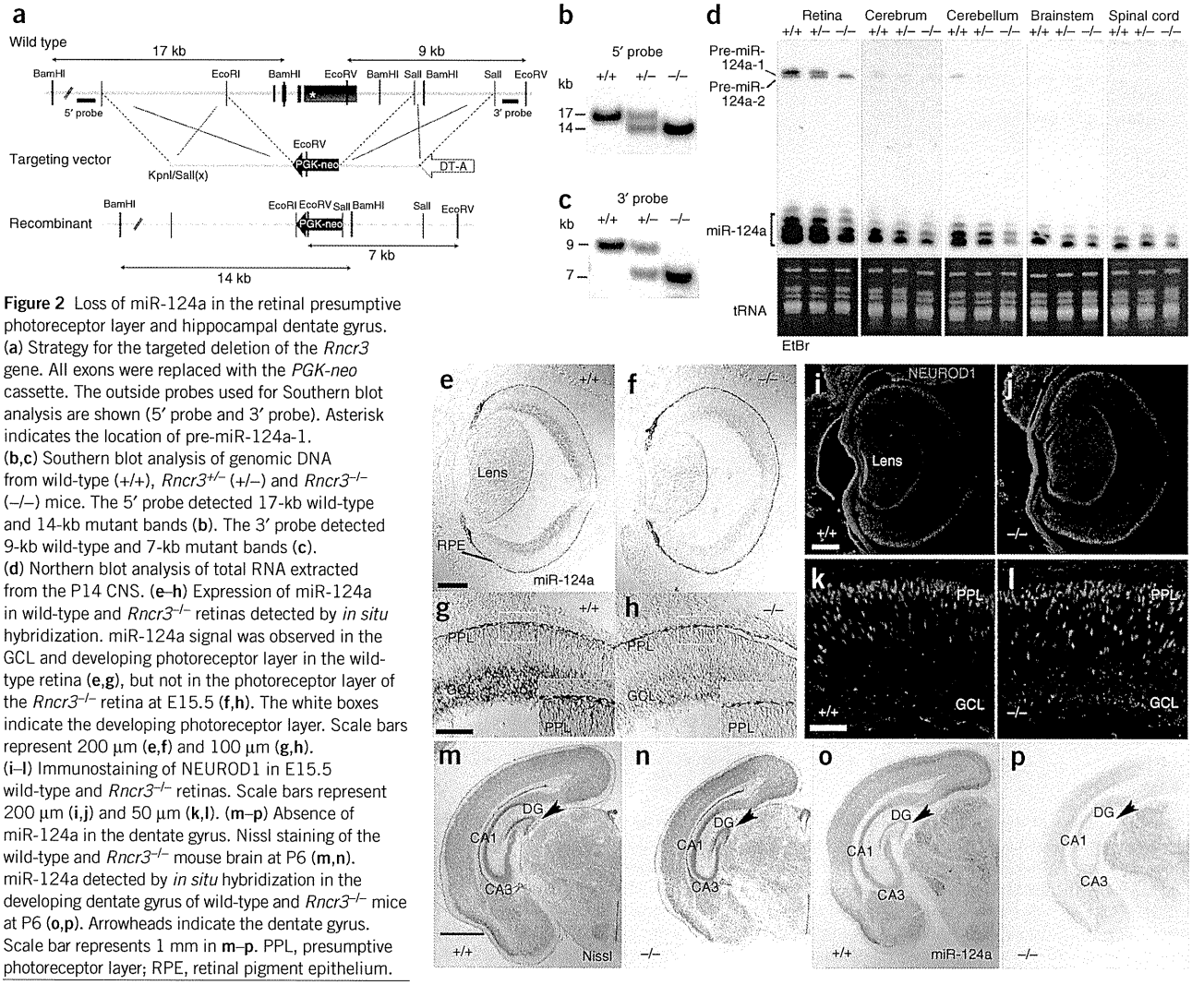


**Figure 2** Loss of miR-124a in the retinal presumptive photoreceptor layer and hippocampal dentate gyrus. (**a**) Strategy for the targeted deletion of the *Rncr3* gene. All exons were replaced with the *PGK-neo* cassette. The outside probes used for Southern blot analysis are shown (5′ probe and 3′ probe). Asterisk indicates the location of pre-miR-124a-1. (**b**,**c**) Southern blot analysis of genomic DNA from wild-type (+/+), *Rncr3*$^{+/-}$ (+/–) and *Rncr3*$^{-/-}$ (–/–) mice. The 5′ probe detected 17-kb wild-type and 14-kb mutant bands (**b**). The 3′ probe detected 9-kb wild-type and 7-kb mutant bands (**c**). (**d**) Northern blot analysis of total RNA extracted from the P14 CNS. (**e**–**h**) Expression of miR-124a in wild-type and *Rncr3*$^{-/-}$ retinas detected by *in situ* hybridization. miR-124a signal was observed in the GCL and developing photoreceptor layer in the wild-type retina (**e**,**g**), but not in the photoreceptor layer of the *Rncr3*$^{-/-}$ retina at E15.5 (**f**,**h**). The white boxes indicate the developing photoreceptor layer. Scale bars represent 200 μm (**e**,**f**) and 100 μm (**g**,**h**). (**i**–**l**) Immunostaining of NEUROD1 in E15.5 wild-type and *Rncr3*$^{-/-}$ retinas. Scale bars represent 200 μm (**i**,**j**) and 50 μm (**k**,**l**). (**m**–**p**) Absence of miR-124a in the dentate gyrus. Nissl staining of the wild-type and *Rncr3*$^{-/-}$ mouse brain at P6 (**m**,**n**). miR-124a detected by *in situ* hybridization in the developing dentate gyrus of wild-type and *Rncr3*$^{-/-}$ mice at P6 (**o**,**p**). Arrowheads indicate the dentate gyrus. Scale bar represents 1 mm in **m**–**p**. PPL, presumptive photoreceptor layer; RPE, retinal pigment epithelium.

© 2011 Nature America, Inc. All rights reserved.

observed a significant reduction of the cone cell number and of mRNA expression of cone-specific genes ($P < 0.001$; **Fig. 3a–d**). To evaluate the physiological function of the *Rncr3*$^{-/-}$ retina *in vivo*, we recorded scotopic and photopic electroretinograms (ERGs) from 2-month-old wild-type and *Rncr3*$^{-/-}$ mice. Both the waveforms and amplitudes of a- and b-waves of scotopic ERGs were very similar between wild-type and *Rncr3*$^{-/-}$ mice (**Fig. 3e–g**). In contrast, the amplitudes of the photopic ERGs of *Rncr3*$^{-/-}$ mice were significantly smaller than those of wild-type mice at all stimulus intensities ($P < 0.05$; **Fig. 3h–j**). The amplitudes of the a-waves, which originate from cone photoreceptors, were less than one-third of those of wild-type mice. Moreover, we found that some opsin-positive cone cells were ectopically localized in the *Rncr3*$^{-/-}$ retina (**Supplementary Fig. 3a–g**). We also examined the development of other retinal cell types in 2-month-old *Rncr3*$^{-/-}$ mouse retinas by immunostaining (**Supplementary Fig. 4a–g**). Rod photoreceptor cells, bipolar cells, amacrine cells, horizontal cells, ganglion cells and Müller glial cells were unaffected. These results indicate that cone photoreceptors are impaired in *Rncr3*$^{-/-}$ mice.

In the developing mouse retina, the expression of TRβ2, an early cone marker, peaks at E17.5 (ref. 16). We examined the number of TRβ2-positive cells in the *Rncr3*$^{-/-}$ retina (**Supplementary Fig. 5a–c**). The number of cones was unaltered in the *Rncr3*$^{-/-}$ retina at E17.5 (**Supplementary Fig. 5c**). Notably, we found some mis-localized TRβ2-positive cells in the E17.5 mutant retina (**Supplementary Fig. 5b**). We then examined the expression of *Crx* and *Otx2*, photoreceptor cell differentiation genes[17–19], and *Neurogenin 2* (*Ngn2*, also known as *Neurog2*), a proneural gene, in both the wild-type and *Rncr3*$^{-/-}$ retinas at E13.5 by *in situ* hybridization and qPCR analysis (**Supplementary Fig. 5d–n**). In contrast with our cone number results, we found no apparent effect on early neurogenesis by quantitatively measuring *Neurod1*, *Trβ2*, *Crx*, *Otx2* and *Ngn2* in wild-type and *Rncr3*$^{-/-}$ retinas, although miR-124a expression was reduced (**Figs. 2i–m** and **3a–d** and **Supplementary Fig. 5a–n**). We examined apoptosis by TUNEL assay in wild-type and *Rncr3*$^{-/-}$ retinas, and found that the number of TUNEL-positive cells was significantly increased in the P3 *Rncr3*$^{-/-}$ retina ($P < 0.05$; **Supplementary Fig. 6a–c**). We further observed an increase in the number of TRβ2 and active caspase-3 double-positive cells and a decrease in the number of TRβ2-positive, caspase-3–negative cells in the *Rncr3*$^{-/-}$ retina (**Fig. 3k–p**), suggesting that the number of cone cells was reduced by apoptosis after neurogenesis. Furthermore, a recent study found that miR-124a was substantially reduced in anaplastic astrocytomas[20]. Thus, we

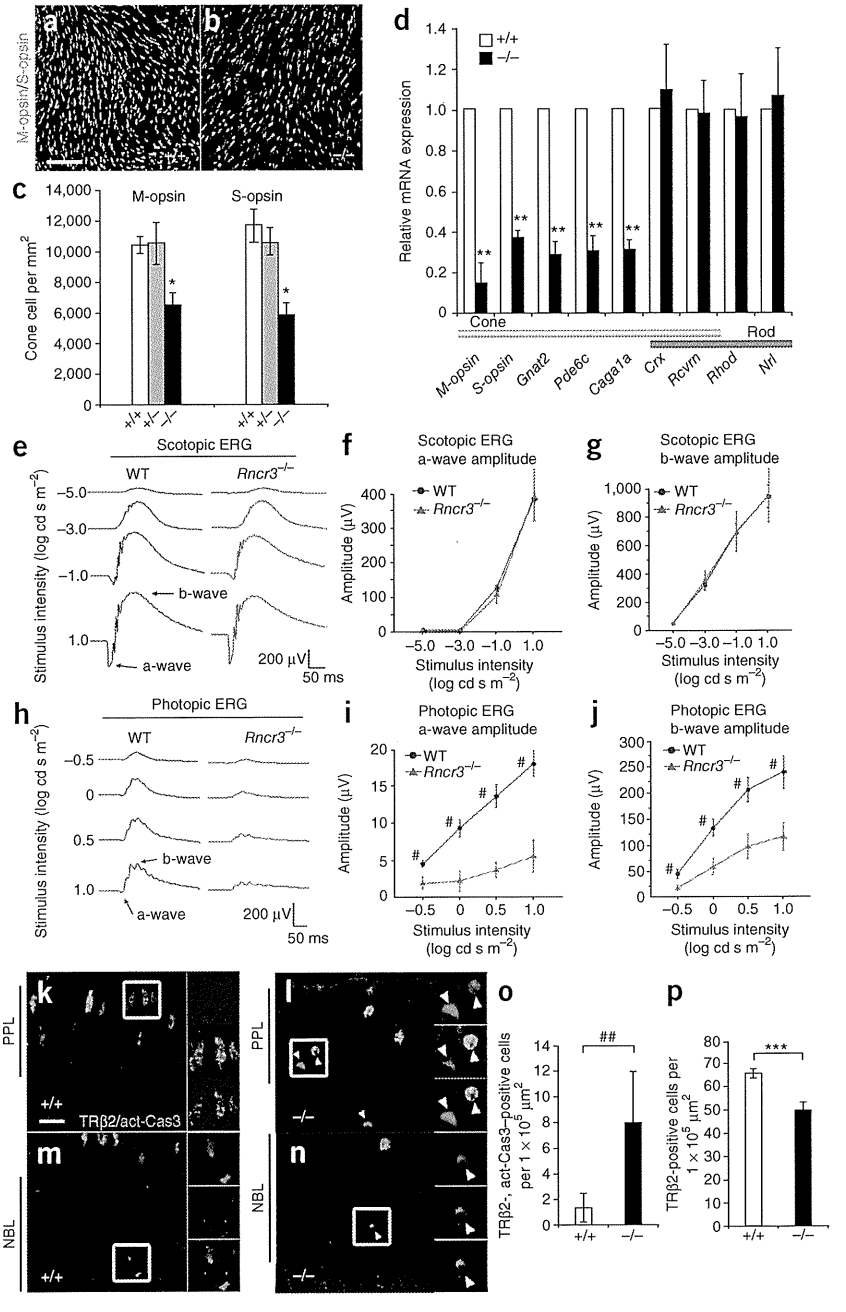


**Figure 3** Reduction of cone photoreceptor cells in the *Rncr3*$^{-/-}$ retina. (**a–c**) Flat-mount immunostaining of central regions of wild-type (**a**) and *Rncr3*$^{-/-}$ (**b**) retinas using antibody to M-opsin (magenta) and antibody to S-opsin (green). Scale bar represents 50 μm. The number of cone cells expressing M-opsin and/or S-opsin in wild-type, *Rncr3*$^{+/-}$ and *Rncr3*$^{-/-}$ retinas are shown in **c** (*$P < 0.001$). Error bars represent s.d. from the means of triplicates. (**d**) Quantitative RT-PCR of retinal photoreceptor genes at P14 (**$P < 0.01$). Error bars represent s.d. from the means of three littermate pairs. *Actb* was used for normalization. (**e–j**) ERGs recorded from 2-month-old wild-type and *Rncr3*$^{-/-}$ mice. Scotopic ERGs elicited by four different stimulus intensities are shown in **e**. The amplitudes of the scotopic ERG a-wave (**f**) and the b-wave (**g**) are shown as a function of the stimulus intensity. Photopic ERGs elicited by four different stimulus intensities are shown in **h**. The amplitude of the photopic ERG a-wave (**i**) and the b-wave (**j**) are shown as a function of the stimulus intensity. Error bars represent s.e.m. (#$P < 0.05$). (**k–p**) Immunostaining of active caspase-3 (act-Cas3) and TRβ2 in the *Rncr3*$^{-/-}$ retina at P3. Arrowheads indicate active caspase-3 and TRβ2 double-positive cells. The white boxes indicate the area enlarged in the right panels. Scale bar represents 10 μm (**k–n**). The number of active caspase-3 and TRβ2 double-positive cells (**o**) and of TRβ2-positive cells (**p**) are shown. Error bars represent s.d. from the means of triplicates. ##$P < 0.02$, ***$P < 0.002$.

examined cell proliferation in the *Rncr3*$^{-/-}$ retina by immunostaining with phosphohistone H3 (PH3) and Ki67 and counting the number of PH3-positive cells at P3 (**Supplementary Fig. 7a–c**). The proportion of PH3-positive cells was not significantly different between wild-type and *Rncr3*$^{-/-}$ retinas ($P > 0.9$). These results suggest that miR-124a is necessary for proper survival and localization of cone cells rather than for early neurogenesis.

We found that 2-month-old *Rncr3*$^{-/-}$ mice had smaller brain weights than did wild types (**Fig. 4a,b**). The small brain phenotype was not apparent at P1, but became significant by P6 during maturation ($P < 0.005$, data not shown). Furthermore, *Rncr3*$^{-/-}$ mice exhibited a front and hind limb clasping response in the tail-suspension assay at 4–5 months (**Fig. 4c,d**). This abnormal phenotype is commonly observed in mouse models of neurodegenerative disorders[21], suggesting that the neural function of the *Rncr3*$^{-/-}$ mouse is substantially impaired. We then performed Timm staining on P10 wild-type and *Rncr3*$^{-/-}$ brain sections, the time at which mossy fibers develop[22], to examine dentate granule cell maturation (**Fig. 4e–h**). Notably, aberrant outgrowth of mossy fibers (dentate granule cell axons) into the CA3 region was observed in the *Rncr3*$^{-/-}$ mouse (**Fig. 4g,h**). The number of apoptotic cells in the dentate gyrus and cortex at P6 was significantly increased (dentate gyrus: wild type, 1.2 ± 1.6 cells per section; *Rncr3*$^{-/-}$, 10.2 ± 3.6; $P < 0.001$; cortex: wild type, 5.8 ± 2.5 cells per $5 \times 10^5$ μm$^2$; *Rncr3*$^{-/-}$, 59.4 ± 17.1; $P < 0.001$; **Fig. 4i–l**). Cell proliferation in the dentate gyrus of *Rncr3*$^{-/-}$ mice was not substantially affected (**Supplementary Fig. 7d,e**), suggesting that apoptosis of neurons contributes to the smaller brain size in *Rncr3*$^{-/-}$ mice. These results indicate that miR-124a is necessary for proper brain development and axogenesis of dentate granule neurons to the CA3.

## Lhx2 is a direct target mRNA of miR-124a *in vivo*

To identify miR-124a target mRNAs, we searched for 3′ untranslated regions (UTRs) of genes that are highly expressed in retinal progenitors and substantially downregulated on progenitor differentiation[23], such as *Lhx2*, *Sox2*, *Rax*, *Six6*, *Six3*, *Pax2*, *Pax6*, *Vsx2* and *Otx2*, using TargetScan 5.1 (http://www.targetscan.org/). Searching the database revealed that *Lhx2* contains an evolutionarily

© 2011 Nature America, Inc. All rights reserved.

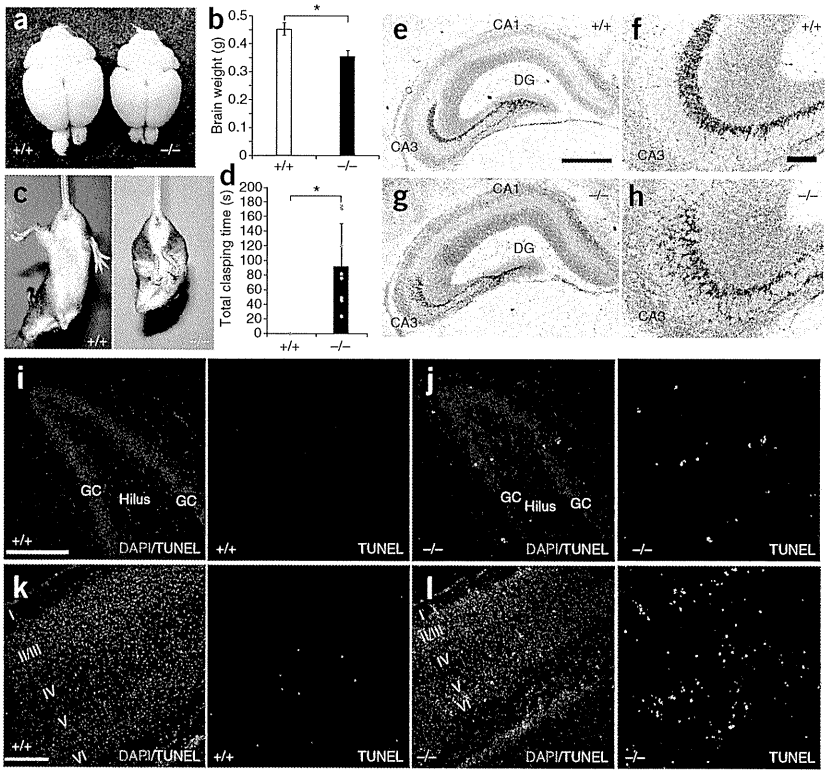


**Figure 4** *Rncr3*$^{-/-}$ mice exhibit neuronal dysfunction and aberrant growth of dentate granule cell axon. (**a**,**b**) Appearance of the brain and brain weight in wild-type and *Rncr3*$^{-/-}$ mice. Representative brains from wild-type (left) and *Rncr3*$^{-/-}$ mice (right, litter mates, 2 months old) are shown in **a**. Brain weights of wild-type ($n = 5$) and *Rncr3*$^{-/-}$ mice ($n = 9$) are shown in **b** (*$P < 0.001$). Error bars represent s.d. (**c**,**d**) Abnormal limb-clasping of *Rncr3*$^{-/-}$ mouse. A clasping response was observed in the *Rncr3*$^{-/-}$ mouse (**c**, right), but not in the wild-type mouse (**c**, left). Total clasping time was measured for 3 min (**d**). Error bars represent s.d. from the mean of $n = 4$ (wild type) and $n = 8$ (*Rncr3*$^{-/-}$). (**e**–**h**) Aberrant sprouting of mossy fibers in the *Rncr3*$^{-/-}$ mouse. The mossy fiber terminals were visualized by Timm staining with Nissl counterstaining at P10. Scale bars represent 500 μm (**e**,**g**) and 100 μm (**f**,**h**). (**i**,**j**) TUNEL assay of the P6 wild-type and *Rncr3*$^{-/-}$ dentate gyrus. Scale bars represent 200 μm. (**k**,**l**) TUNEL assay of the P6 wild-type and *Rncr3*$^{-/-}$ visual cortex. Scale bars represent 200 μm. GC, granule cell layer.

highly conserved miR-124a target sequence (**Fig. 5a**). We examined whether *Lhx2* is a target mRNA of miR-124a by constructing luciferase reporter plasmids that contained native or mutated seed sequences of the *Lhx2* 3′ UTR (**Fig. 5a**) and co-transfecting these reporter plasmids with miR-124a expression plasmids (*pBAsi-mU6-miR-124a-1*, *pBAsi-mU6-miR-124a-2* or *pBAsi-mU6-miR-124a-3*) into HEK 293T cells that lacked endogenous miR-124a (**Supplementary Fig. 8a,b**). HEK 293T cells transfected with miR-124a expression plasmids produced significant amounts of miR-124a ($P < 0.001$; **Supplementary Fig. 8a,b**). The luciferase activity of the native *Lhx2* 3′-UTR plasmid was significantly reduced by all of the pre-miR-124a expression plasmids ($P < 0.01$; **Fig. 5b**). However, luciferase activity of the mutated *Lhx2* 3′-UTR plasmid was not attenuated by miR-124a (**Fig. 5b**), and the luciferase mRNA levels of both native and mutated *Lhx2* 3′-UTR plasmids were not significantly reduced ($P < 0.004$; **Supplementary Fig. 8c,d**). We observed a statistically significant increase of luciferase activity in *Rncr3*$^{-/-}$ hippocampal neurons transfected with native Lhx2 3′-UTR plasmid ($P < 0.009$), but found no significant effect in neurons transfected with the mutated *Lhx2* 3′-UTR plasmid ($P > 0.45$; **Supplementary Fig. 8e**). Next, to determine whether *Lhx2* is an *in vivo* target of miR-124a, we performed immunostaining of the E17.5 *Rncr3*$^{-/-}$ retina using antibodies to LHX2 and TRβ2 antibodies (**Fig. 5c–e**). The number of LHX2 and TRβ2 double-positive cells was significantly increased in the *Rncr3*$^{-/-}$ retina compared with the wild-type retina ($P < 0.01$; **Fig. 5e**). We then introduced *Lhx2* expression plasmids that contained native or mutated 3′ UTR (*Lhx2-Nat* and *Lhx2-Mut*) together with an *egfp* expression plasmid into the P0 mouse retina by *in vivo* electroporation to determine whether retinal cell apoptosis occurs by *Lhx2* overexpression. The number of TUNEL-positive cells was increased in retina transfected with the *Lhx2-Mut* plasmid, but transfection with the *Lhx2-Nat* plasmid did not lead to an increase in the number of TUNEL-positive cells (**Fig. 5f–h**), suggesting that the native 3′ UTR was targeted by native miR-124a. This result is consistent with the observation that the number of TUNEL-positive cells was significantly increased in the *Rncr3*$^{-/-}$ retina ($P < 0.05$; **Supplementary Fig. 6a–c**). These results suggest that *Lhx2* mRNA is a miR-124a target in the retina and that downregulation of *Lhx2* mRNA by miR-124a is necessary for retinal cell survival.

*Lhx2* is known to be required for hippocampal formation[24]. We therefore conducted immunostaining on the dentate gyrus with antibodies to LHX2 and the dentate gyrus marker PROX1. The number of LHX2 and PROX1 double-positive cells was significantly increased in the *Rncr3*$^{-/-}$ dentate gyrus ($P < 0.001$; **Fig. 5i–k**). Furthermore, we compared the expression of *Rncr3* and *Lhx2* mRNA and LHX2 protein in the E12.5 forebrain and P3 retina (**Supplementary Fig. 8f–o**). At E12.5, *Lhx2* mRNA was highly expressed in both the hippocampus and thalamus, whereas *Rncr3* was highly expressed only in the thalamus. In both the developing brain and retina, LHX2 protein was not expressed in regions in which both *Lhx2* and *Rncr3* mRNA were expressed, suggesting that miR-124a targets *Lhx2* mRNA both in the retina and the brain and that miR-124a inhibits translation of *Lhx2* mRNA. Cell density was significantly higher in the dentate gyrus in *Rncr3*$^{-/-}$ mice than in wild-type mice, as determined by counting PROX1-positive cells ($P < 0.004$; **Fig. 5i,j,l**). To assess the role of *Lhx2* in aberrant mossy fiber sprouting, we electroporated *Lhx2-Nat* and *Lhx2-Mut* plasmids into primary cultured hippocampal cells. Substantial neurite extension was observed in cells expressing *Lhx2-Mut* (**Fig. 5m–o**). To evaluate axonal elongation in dentate granule cells, we immunostained hippocampal PROX1 neurons and then measured the axonal length of PROX1-positive cells (**Fig. 5p,q**). The percentage of neurons that contained longer axons, greater than 150 μm in length, was increased by expression of *Lhx2-Mut* (**Fig. 5p**). Furthermore, the average length of the neurons in the top 25$^{th}$ percentile of the population was also significantly increased in *Lhx2-Mut*–expression neurons ($P < 0.05$; **Fig. 5q**). We ectopically expressed *Lhx2* using lentivirus in P6 rat dentate gyrus in slice culture and found that *Lhx2*-transduced dentate granule cells extended longer

© 2011 Nature America, Inc. All rights reserved.

axons to the CA3 region by 5 d *in vitro* (DIV) than the wild-type cells (**Fig. 5r–u**). These results suggest that a proper LHX2 protein level, which is affected by miR-124a, is required for the appropriate development of axons in the dentate gyrus.

### Rescue of *Rncr3*$^{-/-}$ mice by pre-miR-124a-2 or *Lhx2* knockdown

To determine whether miR-124a is responsible for the *Rncr3*$^{-/-}$ retinal phenotype, we carried out a rescue experiment by mating *Rncr3*$^{-/-}$ mice with transgenic mice that specifically expressed miR-124a in

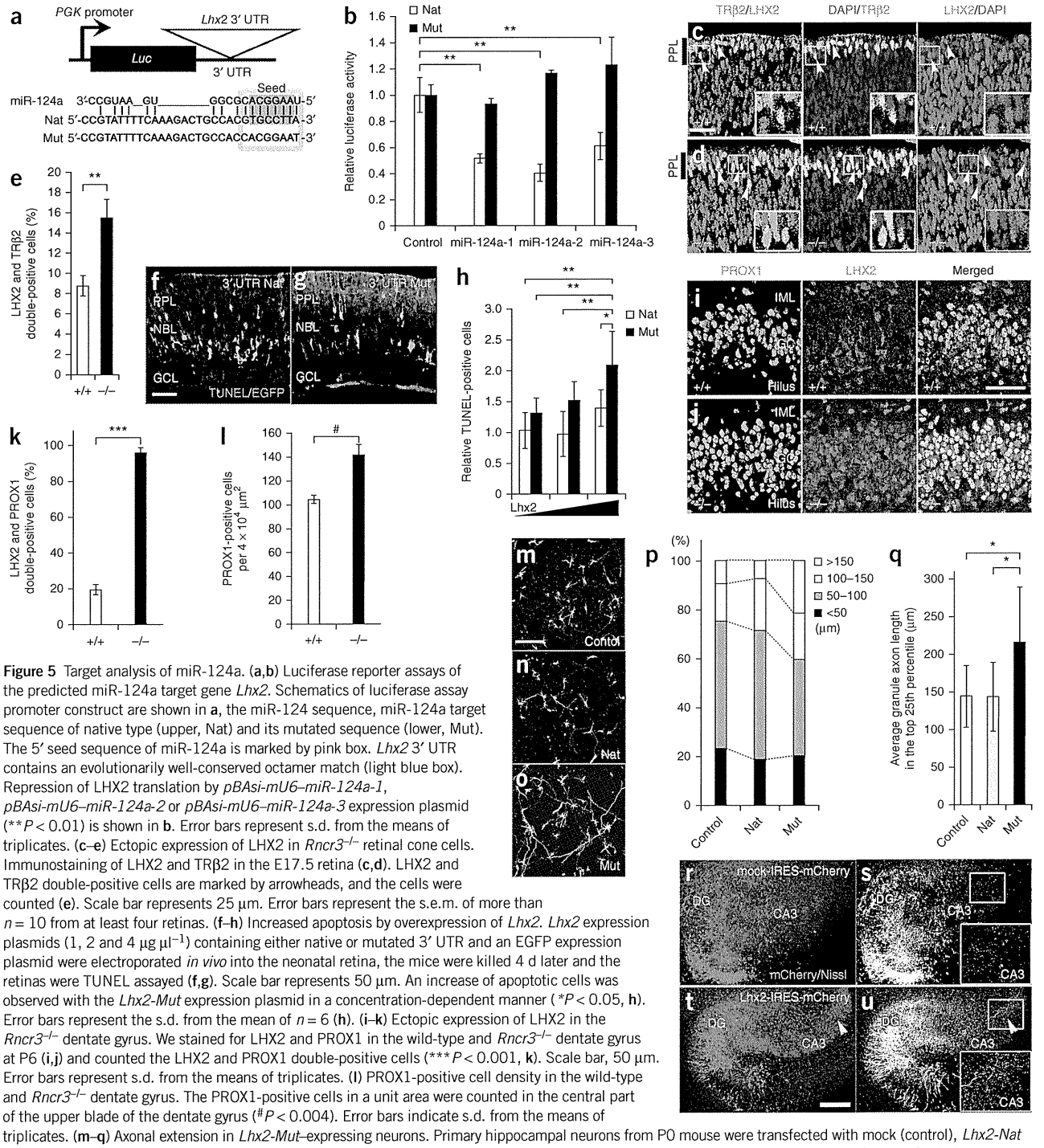


**Figure 5** Target analysis of miR-124a. (**a**,**b**) Luciferase reporter assays of the predicted miR-124a target gene *Lhx2*. Schematics of luciferase assay promoter construct are shown in **a**, the miR-124 sequence, miR-124a target sequence of native type (upper, Nat) and its mutated sequence (lower, Mut). The 5′ seed sequence of miR-124a is marked by pink box. *Lhx2* 3′ UTR contains an evolutionarily well-conserved octamer match (light blue box). Repression of LHX2 translation by *pBAsi-mU6–miR-124a-1*, *pBAsi-mU6–miR-124a-2* or *pBAsi-mU6–miR-124a-3* expression plasmid (**$P < 0.01$) is shown in **b**. Error bars represent s.d. from the means of triplicates. (**c**–**e**) Ectopic expression of LHX2 in *Rncr3*$^{-/-}$ retinal cone cells. Immunostaining of LHX2 and TRβ2 in the E17.5 retina (**c**,**d**). LHX2 and TRβ2 double-positive cells are marked by arrowheads, and the cells were counted (**e**). Scale bar represents 25 μm. Error bars represent the s.e.m. of more than $n = 10$ from at least four retinas. (**f**–**h**) Increased apoptosis by overexpression of *Lhx2*. *Lhx2* expression plasmids (1, 2 and 4 μg μl$^{-1}$) containing either native or mutated 3′ UTR and an EGFP expression plasmid were electroporated *in vivo* into the neonatal retina, the mice were killed 4 d later and the retinas were TUNEL assayed (**f**,**g**). Scale bar represents 50 μm. An increase of apoptotic cells was observed with the *Lhx2-Mut* expression plasmid in a concentration-dependent manner (*$P < 0.05$, **h**). Error bars represent the s.d. from the mean of $n = 6$ (**h**). (**i**–**k**) Ectopic expression of LHX2 in the *Rncr3*$^{-/-}$ dentate gyrus. We stained for LHX2 and PROX1 in the wild-type and *Rncr3*$^{-/-}$ dentate gyrus at P6 (**i**,**j**) and counted the LHX2 and PROX1 double-positive cells (***$P < 0.001$, **k**). Scale bar, 50 μm. Error bars represent s.d. from the means of triplicates. (**l**) PROX1-positive cell density in the wild-type and *Rncr3*$^{-/-}$ dentate gyrus. The PROX1-positive cells in a unit area were counted in the central part of the upper blade of the dentate gyrus ($^{\#}P < 0.004$). Error bars indicate s.d. from the means of triplicates. (**m**–**q**) Axonal extension in *Lhx2-Mut*–expressing neurons. Primary hippocampal neurons from P0 mouse were transfected with mock (control), *Lhx2-Nat* (native), *Lhx2-Mut* (mutated) together with EGFP by electroporation. Confocal microimages of neurons 72 h after transfection are shown in **m**–**o**. Scale bar represents 200 μm. The percentages of axons with lengths ≤50, 50–100, 100–150 and >150 μm from $n = 85$ (control), 81 (nat), and 89 (mut) neurons are shown in **p**. The average axon lengths in the top 25% percentile are shown in **q**. Error bars represent s.d. (**r**–**u**) Lentivirus-infected hippocampal slice culture. Shown are confocal images of the P6, 5 DIV sliced rat hippocampus infected with mock (control, **r**,**s**) or *Lhx2* (**t**,**u**) expression virus. The small white boxes in **s** and **u** are the CA3 regions, magnified in the bottom right corner. Arrowheads indicate elongated mossy fibers in the CA3. Scale bar represents 200 μm. IML, inner molecular layer.

© 2011 Nature America, Inc. All rights reserved.

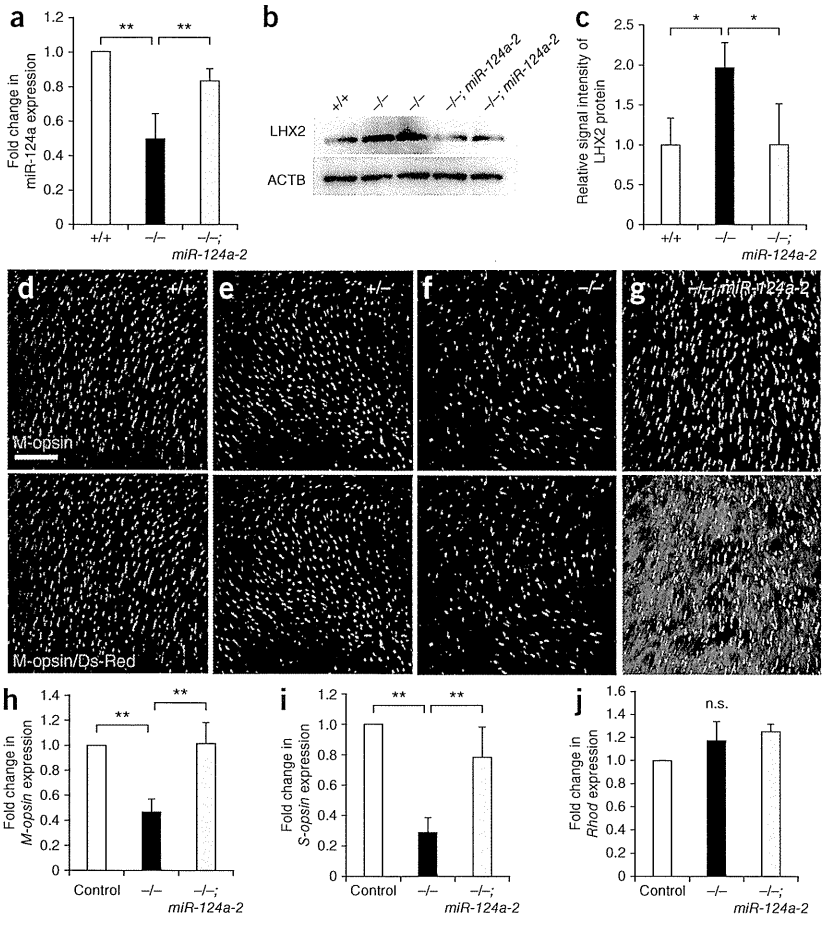


**Figure 6** *In vivo* rescue experiments of *Rncr3*$^{-/-}$ mice by miR-124a expression in the retina. (**a**) Expression of miR-124a in the wild-type, *Rncr3*$^{-/-}$ and *Rncr3*$^{-/-}$; *Crx–miR-124a-2* retinas (**$P < 0.01$). Error bars represent the s.d. from the mean of triplicate (wild type and *Rncr3*$^{-/-}$) and $n = 4$ (*Rncr3*$^{-/-}$; *Crx–miR-124a-2*). (**b**,**c**) Comparison of LHX2 protein levels in the wild-type, *Rncr3*$^{-/-}$ and *Rncr3*$^{-/-}$; *Crx–miR-124a-2* retina. Western blots of LHX2 in the retina are shown in **b**. ACTB (β-actin) was used as a loading control. The signal intensity of LHX2 protein is shown in **c** (*$P < 0.05$). Error bars represent the s.d. from the means of triplicates (wild type) and $n = 4$ (*Rncr3*$^{-/-}$ and *Rncr3*$^{-/-}$; *Crx–miR-124a-2*). (**d–g**) Rescue of decreased cone cells by miR-124a expression. Flat-mount immunostaining using antibody to M-opsin (green). The *pre-miR-124a-2* transgene also expressed Ds-Red (magenta) as a marker. Scale bar represents 50 μm. (**h–j**) Real-time qRT-PCR analysis of control (+/+; *Crx–miR-124a-2* and *Rncr3*$^{+/-}$; *Crx–miR-124a-2*), *Rncr3*$^{-/-}$ and *Rncr3*$^{-/-}$; *Crx–miR-124a-2* transgenic retinas. Intron-spanning primers amplifying mouse *M-opsin* (also known as *Opn1mw*, **h**), *S-opsin* (also known as *Opn1sw*, **i**), *Rho* (**j**), and *Actb* were used for normalization. Error bars represent the s.d. from the means of three independent littermate pairs. **$P < 0.01$; n.s., not significant, $P > 0.05$.

photoreceptor cells using a *Ds-Red-intron-miR-124a-2* expression cassette driven by 2.3 kb of the *Crx* promoter[5,25] (*Crx–miR-124a-2*; **Supplementary Fig. 9a**). In the P1 retina, we observed that both miR-124a expression and the LHX2 protein level reverted back to those of control mice (**Fig. 6a–c**). We then performed flat-mount immunostaining (**Fig. 6d–g**) and conducted qPCR analysis on retinal photoreceptor marker genes using the adult retina (**Fig. 6h–j**). Both the decreased cone cell numbers and gene expression in the *Rncr3*$^{-/-}$ retina were restored to normal levels when transgenic pre-miR-124a-2 was expressed (**Fig. 6d–i**). The number of mislocalized cone cells also recovered (**Supplementary Fig. 9b–i**). These results suggest that the cone cell reduction and mislocalization in the *Rncr3*$^{-/-}$ retina are the results of miR-124a-1 disruption and that the primary function of *Rncr3* is to encode miR-124a.

To determine whether the loss of miR-124a is also responsible for the brain phenotypes, we generated a transgenic mouse that expresses *Ds-Red-intron-miR-124a-2* in postmitotic neurons, driven by 4.3 kb of the *synapsin 1* promoter (*Syn1–miR-124a-2*)[26] (**Supplementary Fig. 10a–c**). We performed an *in situ* hybridization of miR-124a and immunostained for LHX2 in the P10 brain. In the dentate gyrus of the *Rncr3*$^{-/-}$; *Syn1–miR-124a-2* mice, both the reduced level of mature miR-124a and the elevated level of LHX2 protein that we observed in *Rncr3*$^{-/-}$ mice were restored to similar levels as seen in control mice (**Fig. 7a–f**). In addition, the number of apoptotic cells was significantly reduced in the brains of *Rncr3*$^{-/-}$; *Syn1–miR-124a-2* mice compared with *Rncr3*$^{-/-}$ mice ($P < 0.01$; **Supplementary Fig. 10d**). In *Rncr3*$^{-/-}$; *Syn1–miR-124a-2* mice, Timm-stained mossy fiber axonal terminals incompletely, but substantially, recovered from aberrant sprouting into the CA3 region (**Fig. 7g–l**). The other phenotypes, including brain weight, clasping and apoptosis in the cortex, were not substantially rescued in *Rncr3*$^{-/-}$; *Syn1–miR-124a-2* mice (data not shown). This partial rescue may be a result of insufficient expression and/or inappropriate expression timing of the miR-124a transgene.

To determine whether downregulation of *Lhx2* can rescue the *Rncr3*$^{-/-}$ phenotype, we constructed a short hairpin RNA (shRNA) to knockdown *Lhx2* (*shLhx2*; **Supplementary Fig. 11a,b**). We transfected *shLhx2* into organ-cultured P0 retina using a recombinant adeno-associated virus serotype 5 (AAV5; **Supplementary Fig. 11c**). After 5 DIV, we performed immunostaining using an antibody to S-opsin. In the 5 DIV *Rncr3*$^{-/-}$ retina, the number of cone cells was reduced in retina transfected with control shRNA (shControl), whereas the number of cone cells was significantly increased in retina transfected with *shLhx2* compared with the control ($P < 0.01$; **Fig. 8a–e**). The number of cone cells in *shLhx2*-infected wild-type retina was unaltered (**Fig. 8a,c**), suggesting that the *Lhx2* knockdown rescue phenotype is not a result of an off-target effect. In addition, we forced the expression of shLhx2 in primary cultured hippocampal neurons to determine whether downregulation of *Lhx2* can rescue *Rncr3*$^{-/-}$ dentate gyrus neuron axonal elongation (**Fig. 8f–j**). The average dentate granular axon length in the neurons in the top 25$^{th}$ percentile of the population (determined by axon length) was significantly increased in shControl-transfected *Rncr3*$^{-/-}$ dentate gyrus neurons ($P < 0.01$; **Fig. 8g**). The elongated *Rncr3*$^{-/-}$ dentate gyrus axon phenotype was restored to the wild-type level by transfection of *shLhx2* (**Fig. 8i,j**). These results suggest that *Lhx2* is a primary target gene of miR-124a and is responsible for the *Rncr3*$^{-/-}$ phenotypes, including both the reduction of retinal cone cell numbers and mossy fiber elongation of the dentate gyrus.

© 2011 Nature America, Inc. All rights reserved.